Using Radar Data to Calibrate a Stochastic Parametrization of Organized Convection

Cardoso-Bihlo, E., Khouider, B., Schumacher, C., & De La Chevrotière, M.

2019

JAMES | Journal of Advances in Modeling Earth Systems

RESEARCH ARTICLE
10.1029/2018MS001537

Using Radar Data to Calibrate a Stochastic Parametrization of Organized Convection

E. Cardoso-Bihlo[1,2], B. Khouider[1], C. Schumacher[3], and M. De La Chevrotière[4]

[1]Department of Mathematics and Statistics, University of Victoria, Victoria, British Columbia, Canada, [2]Now at Mathematics and Statistics, Memorial University of Newfoundland, St. John's, Newfoundland and Labrador, Canada, [3]Department of Atmospheric Sciences, Texas A&M University, College Station, TX, USA, [4]Environment and Climate Change Canada, Dorval, Quebec, Canada

Key Points:
- A Bayesian method is used to infer key parameters for a stochastic multicloud model from radar data
- SMART-R radar rain types were combined with DYNAMO soundings as convection predictors
- Inferred parameters and simulated cloud area fractions were validated and compared to previous studies

Correspondence to:
B. Khouider,
khouider@uvic.ca

Citation:
Cardoso-Bihlo, E., Khouider, B., Schumacher, C., & De La Chevrotière, M. (2019). Using radar data to calibrate a stochastic parametrization of organized convection. *Journal of Advances in Modeling Earth Systems*, *11*, 1655–1684. https://doi.org/10.1029/2018MS001537

Received 23 OCT 2018
Accepted 28 APR 2019
Accepted article online 9 MAY 2019
Published online 19 JUN 2019

Abstract Stochastic parameterizations are increasingly becoming skillful in representing unresolved atmospheric processes for global climate models. The stochastic multicloud model, used to simulate the life cycle of the three most common cloud types (cumulus congestus, deep convective, and stratiform) in tropical convective systems, is one example. In this model, these clouds interact with each other and with their environment according to intuitive-probabilistic rules determined by a set of predictors, depending on the large-scale atmospheric state and a set of transition time scale parameters. Here we use a Bayesian statistical method to infer these parameters from radar data. The Bayesian approach is applied to precipitation data collected by the Shared Mobile Atmospheric Research and Teaching Radar truck-mounted C-band radar located in the Maldives archipelago, while the corresponding large-scale predictors were derived from meteorological soundings taken during the Dynamics of the Madden-Julian Oscillation field campaign. The transition time scales were inferred from three different phases of the Madden-Julian Oscillation (suppressed, initiation, and active) and compared with previous studies. The performance of the stochastic multicloud model is also assessed, in a stand-alone mode, where the cloud model is forced directly by the observed predictors without feedback into the environmental variables. The results showed a wide spread in the inferred parameter values due in part to the lack of the desired sensitivity of the model to the predictors and the shortness of the training periods that did not include both active and suppressed convection phases simultaneously. Nonetheless, the resemblance of the stand-alone simulated cloud fraction time series to the radar data is encouraging.

1. Introduction

According to IPCC reports (IPCC, 2013, 2007), anthropogenic influence is in large part responsible for the recent observed changes in the climate and environmental systems. The most prominent change is the increase of the global average temperature, which is likely associated with the release of greenhouse gases in the atmosphere (IPCC, 2013). Studies suggest that the warming of the atmosphere might have an impact on the cloud cover (Bony et al., 2016; Hartmann, 2016; McCoy et al., 2017; Stephens, 2005). Clouds play an important role in our climate system; they interact with solar and terrestrial energy flows through different processes such as the absorption, emission, and reflection of electromagnetic waves and thus produce nontrivial feedbacks on global warming that are still poorly understood (Bony et al., 2016). Moreover, cumulus clouds further affect the energy flows through latent heat and precipitation. The vertical motions within clouds, in particular deep clouds, are responsible for the transport of heat, moisture, and momentum involving multiple scales ranging from mesoscale systems to planetary-scale disturbances such as the Madden-Julian Oscillation (MJO; Hendon, 1993).

Despite the considerable progress that has been made in the representation of clouds in recent years, climate models still present a large spread in cloud feedback, which has been considered as one of the major uncertainties in the estimation of climate sensitivity. The parameterization of certain aspects of cloud processes has been considered as a possible cause for this issue (Bony & Dufresne, 2005; Senior & Mitchell, 1993; Zhang, 2005; Zhao et al., 2016), especially its role and influence on cloud feedback (McCoy et al., 2017; Webb et al., 2015; Zhang MH, 2008) as well as the distinction of the various types of clouds which may contribute to the spread (Zelinka et al., 2012). In fact, low-level clouds in the tropics have been identified as a large contributor to the climate sensitivity spread (IPCC, 2007, 2013). In particular, the poor representation

by climate models of tropical marine stratocumulus and trade cumulus is thought to be the cause of major uncertainties in the simulation of future climate scenarios (Klein et al., 2017).

In Brient and Bony (2013), where the behavior of low clouds is analyzed in different climate models, using the same physical parameterizations under changing climate perturbations (warmer climate), it is found that a strong positive cloud feedback results from the decrease of low-level cloud amount in the tropics in regimes of weak subsidence. It is further stated that the decrease of the amount of low-level clouds is also observed in other experimental studies. In order to understand and address the cloud feedback mechanism in connection with climate change and present as well as future global atmospheric circulation, the cloud feedback model intercomparison project (Webb et al., 2016) has been launched; it supports ongoing intercomparison between models through a corresponding diagnostic code catalog to facilitate the evaluation of clouds and to better understand how physical processes may contribute to errors in climate models (Tsushima et al., 2017).

Although cloud feedback is positive in most Global Climate Models (GCMs), meaning an additional warming of Earth's atmosphere (Brient & Bony, 2013; Ceppi et al., 2017), uncertainties related to the representation of microphyical aspects of clouds remain, as, for example, aerosol distributions, processes related to precipitation, ice, and mixed phase microphysics (Ceppi et al., 2017; Gettleman & Sherwood, 2016; McCoy et al., 2015). These will need to be addressed and further investigated. Since clouds affect not only the weather but also the climate system as a whole through different processes, their accurate representation in GCMs is necessary for future climate projections (Senior & Mitchell, 1993).

Problems associated with the representation of clouds in GCMs are related not only to the limited spatial resolution of the climate model itself but also to the complexity of the many related physical processes, which interact with each other over a wide range of temporal and spacial scales and to the cloud type diversity in the atmosphere (Jakob, 2001; Siebesma et al., 2004). For example, the representation of radiative effects and latent heat demands the representation of processes that occur on much smaller scales than the grid resolution of climate models. Atmospheric processes that are related to phase changes of water and the consumption and release of latent heat require the accurate representation of cloud microphysics. Besides the aspects related to climate prediction, a poor representation of clouds results in biased simulations of precipitation (Kidd et al., 2013; Zhang et al., 2010). Cumulus parameterization schemes, in particular, are typically constructed in such a way that ensemble means, that is, their effect on large-scale dynamics, are well represented but variability that arises from small scales are not accounted for (Lin & Neelin, 2002).

In Palmer (2001), it is argued that the subgrid variability should be part of the parameterization scheme expressed by dynamic-stochastic systems coupled with the resolved system over the different range of scales instead of using deterministic schemes, which are limited by the underlying grid scale. Moreover, neglecting the variability of small scales can lead to errors in the climatology of large-scale variables. For this reason, some researchers have opted for the incorporation of stochastic elements in those schemes. Buizza et al. (1999) showed that ensemble prediction where the parameterized tendencies were perturbed by a stochastic element was more skillful in the probabilistic prediction for precipitation. Lin and Neelin (2003) obtained improved precipitation variance by adding a stochastic perturbation to the convective available energy and the vertical structure of the heating of a traditional convective scheme. Plant and Craig (2008) created a new stochastic convection scheme based on adaptation of the plume closure of the Kain-Fritsch convection scheme to allow the number and size of clouds to randomly vary in a grid box. By comparison with a standard deep parameterization, the Plant-Craig scheme improves the prediction of rainfall of light and medium intensities over large areas (Keane et al., 2016). Bright and Mullen (2002) increased the probabilistic skill and spread for ensemble forecasts by applying a stochastic perturbation to the trigger function of the Kain-Fritsch parameterization scheme. Along the same line, Hagos et al. (2018) proposed a nonequilibrium statistical mechanics model for the size and number of clouds based on their rates of growth and decay as well as the cloud base mass flux and used radar data to calibrate it.

Based on observations that different types of clouds—congestus, deep convective, and stratiform—play a role in the dynamics of convectively coupled Kelvin waves, the MJO, and westward-propagating 2-day waves, a deterministic multicloud model (MCM) parameterization (Khouider & Majda, 2006a, 2006b) was developed based on two convective heating modes (Majda & Shefter, 2001). This new deterministic MCM carries congestus, deep convective, and stratiform cloud types and takes into account convective available potential energy (CAPE) and dryness of the middle troposphere to decide on the type of convection (deep vs.

congestus) to be promoted; when implemented in a climate model, the MCM assumes three heating and cooling profiles to account for the condensational and radiative forcing due to the three cloud types. A half sine-like profile that extends over the entire troposphere is used to account for the diabatic heating from deep convective clouds, and a full sine-like profile is used for both stratiform and congestus clouds according to the intuition that stratiform clouds heat the upper troposphere due to deposition and freezing and cool the lower troposphere due melting and evaporation of stratiform precipitation while congestus clouds heat the lower troposphere due to condensation and cool the upper troposphere due to cloud water detrainment and (reduced) long-wave radiation. The three cloud types thus force directly the first two baroclinic modes according to the linear mode theory. Details can be found in MCM and stochastic MCM (SMCM) papers cited herein.

A new SMCM was introduced in Khouider et al. (2010) to represent the variability associated with unresolved small features of organized tropical convection in state-of-the-art GCMs. This model targets the representation of the lifetime of clouds in the tropical atmosphere. It was introduced as a "stochasticization" of the multicloud parameterization first introduced in Khouider and Majda (2006b). The key idea was to extend the framework of the stochastic interacting lattice model for convective inhibition (CIN; Khouider et al., 2003) to the case of multiple cloud types and devise intuitive-probabilistic rules for their evolution and mutual interactions based on various large-scale predictors. The result is a stochastic birth-death process for the cloud area fractions associated with the aforementioned three cloud types with conditional transition probabilities.

Taking all the known issues of existing parameterizations listed above into account, the SMCM offers an inexpensive way to simulate the birth and death of clouds modulated in terms of a Markov chain process. The SMCM has been successful in improving the simulated features of tropical convection and wave characteristics in an idealized aquaplanet-GCM (Ajayamohan et al., 2016; Deng et al., 2015, 2016). Peters et al. (2017) recently showed that the use of the SMCM to help an existing cumulus scheme in a GCM to better trigger and modulate convection improves the capability of the model to simulate features of tropical intraseasonal variability. Goswami et al. (2017c; see also Goswami et al., 2017b, and Goswami et al., 2017a) implemented the SMCM in the second version of the Climate Forecasting System of the National Centers for Environmental Predictions climate model. They showed that the SMCM leads to major improvements in the simulation of the tropical modes of atmospheric variability such as convectively coupled waves, the MJO, and monsoon intraseasonal variability without deterioration of the mean climatology, which has arguably also seen some minor improvements.

However, the major drawback of the SMCM resides in its use of a large number of tuning parameters to which the results are highly sensitive. Further quantitative improvements in GCM simulations based on the SMCM are subject to a better estimation of those parameters. In a nutshell, the SMCM operates as a probabilistic model that emulates the distributions of various cloud type area fractions conditional on a set of large-scale predictors defined through the GCM variables. As a step forward to reducing the uncertainties in the SMCM parameters, De La Chevrotière et al. (2014, 2016) developed and used a Bayesian inference method to estimate key time scale parameters of the transition probabilities that define the time evolution of the emulated distributions from observations. However, this inference method has so far been applied only to synthetic and large-eddy simulation (LES) data.

The aim of this study is to introduce and preassess a refinement of this SMCM by introducing new dynamical predictors and thus extend the Bayesian inference algorithm developed in De La Chevrotière et al. (2014) to estimate the transition times between the various cloud types. For the estimation of the transition rates, we use measurements from the C-band Shared Mobile Atmospheric Research and Teaching Radar (SMART-R) deployed during the Dynamics and the MJO (DYNAMO), the Cooperative Indian Ocean Experiment on Intraseasonal Variability in the Year 2011 (CINDY2011), and the Atmospheric Radiation Measurement MJO Investigation Experiment (AMIE) field campaigns (DYNAMO/CINDY2011/AMIE; hereafter referred to as DYNAMO; Yoneyama et al., 2013) to determine the observed area fractions of the various cloud types, combined with measurements from the sounding array to represent the large-scale environmental conditions. The preassessment is done through direct comparison of inferred transition time scales to those obtained or used in previous studies and also by comparing the observed cloud area fractions used during the inference procedure with those simulated by the SMCM using the inferred transition time scales and forced by the same array-averaged large-scale predictors from DYNAMO.

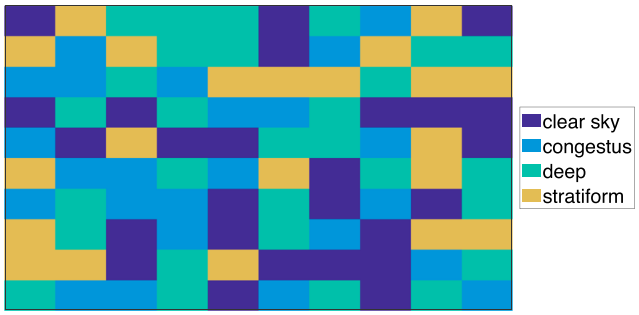

Figure 1. The multicloud model lattice of $n \times n$ sites overlaid on a GCM grid box. Each lattice site is occupied by a congestus, deep, or stratiform cloud type or is a clear sky site.

Modern data science tools are increasingly used by the climate modeling community to improve climate models, and especially cumulus parameterizations, to observations and high-resolution simulation data. The Bayesian paradigm used here is one of them. By contrast, Rasp et al. (2018) and Brenowitz and Bretherton (2018) use machine learning to constrain the convective tendency to high-resolution simulation data based on a multiscale modeling framework and cloud resolving modeling, respectively. See also the work of Gentine et al. (2018) and Schneider et al. (2017).

Section 2 of this paper provides a brief review of the most important features of the SMCM including the modifications of introducing new large-scale predictors as well as the Bayesian inference technique. In section 3, we describe the observational data sets and present the three data subsets that are used to test the Bayesian inference. The results of the Bayesian technique applied to the three testing data subsets are presented and analyzed in section 4. In particular, we compare the transition time scales obtained in each test case with previous studies. Moreover, we assess the performance of the SMCM in a stand-alone mode, where the cloud model is forced by the observed large predictors without feedback to the large-scale dynamics, in terms of its capability to reproduce the observed cloud time series using the corresponding inferred transition time scales. A conclusion is given in section 5.

2. Modeling Framework

2.1. Overview

In this section, we review some of the most important features of the SMCM; introduce new large-scale predictors to accommodate the inhibition of deep convection during a strong inversion, large CIN, and strong large-scale subsidence; and outline the Bayesian inference procedure. A more detailed description of the original MCM and SMCM can be found in a number of previous studies (Khouider et al., 2010; Khouider & Majda, 2006a, 2006b, 2008a, 2008b).

Based on the actual state of the atmosphere, which is characterized in terms of its large-scale variables, the SMCM outputs a time series describing the life cycle of three cloud type (congestus, deep convective, and stratiform) area fractions evolving on a lattice with $n \times n$ sites and overlaid on each GCM grid box. A visual representation of a random configuration of such a lattice, divided into 10×10 sites, is provided in Figure 1. In this setting, each lattice is either occupied by one cloud type or is clear sky. The lattice resolution is on the order of 5 to 10 km, representative of the spatial scale of deep convective clouds. Therefore, the number of lattice sites can vary between 10×10 and 40×40 depending on the GCM grid spacing. In the present version of the SMCM, the lattice sites do not interact with each other. Khouider (2014) developed a new methodology that incorporates the interaction between sites, but it has not been yet implemented in an actual or simplified GCM despite its potential for representing the organization of convection due to unresolved processes such the sea breeze (Bergemann & Jakob, 2016; Bergemann et al., 2017). At any given time, a lattice site in a specific state might switch to a different state according to probability rules, which in turn depend on the large-scale state of the atmosphere.

According to Khouider et al. (2010), certain transitions, such as the transition of stratiform to deep convection or of clear sky directly to stratiform, are deemed forbidden because they are unphysical. Only the transitions represented in the following diagram are allowed, on the infinitesimal time,

$$\begin{array}{ccccc} \text{clear sky} & \longrightarrow & \text{congestus} & \longrightarrow & \text{deep} \\ \downarrow & & \downarrow & & \downarrow \\ \text{deep} & \longrightarrow & \text{clear sky} & \longleftarrow & \text{stratiform}, \end{array}$$

and all other transitions have their transition rates set to zero and thus have a minimal transition probability on relatively short time intervals, consistent with the theory of continuous-time Markov chains.

It is worth noting that throughout this article, stratiform clouds refer only to stratiform precipitating anvils that form in the wake of deep convection. Other forms of stratiform clouds such as stratus, stratocumulus,

and nonprecipitating anvils are not represented here. As such, the model does not account for large-scale stratiform clouds that form in the absence of deep convection (e.g., as might occur in large-scale isentropic lift conditions at middle and higher latitudes), which limits the scope of this model in its present form in terms of representing the distribution of hydrological and radiative effects of clouds globally.

The original model developed by Khouider et al. (2010) uses CAPE and midtropospheric dryness (D) as the large-scale state predictors to determine favorable conditions for tropical convective events. The probabilistic evolution of the cloud area fractions associated with the aforementioned three cloud types is obtained by simulating the coarse-grained birth-death process using the exact "Monte Carlo" algorithm of Gillespie (1975). In the SMCM, the lifetime of each of the clouds is determined by the transition rate equations, which are formulated in terms of the large-scale predictors and prescribed transition time scale parameters (Khouider et al., 2010). The main problem we are addressing is to find the right values for these transition time scales.

In Khouider et al. (2010), two sets of transition time scales were proposed based on physical intuition. In Frenkel et al. (2012), these time scale parameters were minimally tuned to improve the variability and mean climatology of simulated moist gravity waves compared to the deterministic MCM. The SMCM was compared with observations for the first time in Peters et al. (2013), where the statistics of the observed tropical convection were contrasted with the output of the SMCM. That study shows in particular that the simulations of the cloud area fractions from deep convective and stratiform clouds are more realistic when midtropospheric vertical velocity is used instead of purely thermodynamic predictors, that is, CAPE and low-level CAPE, which is obtained from the integration of the buoyancy force throughout the lower troposphere until the freezing level. While this exercise is sensible when one is dealing with observational data, the subtle two-way relationship between convection and vertical velocity makes the use of vertical velocity as a predictor in a GCM parameterization problematic. For moisture and boundary layer dynamics related predictors such as CAPE, CIN, and inversion and even large-scale subsidence used here, there is large time scale separation between convection and their regeneration by various large-scale and boundary layer processes.

In order to reproduce the stochastic behavior of convection in the SMCM and observations, Peters et al. (2013) adjusted the transition time scales based on a visual match between the analytical equilibrium of cloud area fractions of the SMCM and the observed mean deep convective cloud fractions for each of the selected large-scale predictors. In De La Chevrotière et al. (2014), a Bayesian statistical method to infer the transition time scales from data was developed and validated. This Bayesian method was applied in De La Chevrotière et al. (2016) to LES data (Khairoutdinov et al., 2009), and the inferred parameters were used in Goswami et al. (2017a, 2017b, 2017c). These studies used CAPE, low-level CAPE, and dryness as large-scale predictors.

2.2. Introduction of New Large-Scale Predictors in the SMCM: The Extended SMCM

The development of convective events depends on specific atmospheric conditions. The usual procedure to access such conditions is through the analysis of indices characterizing the state of the atmosphere (Holton, 1972). It is important to distinguish between large-scale conditions that trigger convection, sustain convection, and cause convection to cease. Moreover, different phases of convection are associated with different cloud types, as observations of convective systems show (Mapes et al., 2006). One of the most well-known indices characterizing the state of the atmosphere is CAPE, which is often associated with the severity of deep convection. It is a measure of deep instability in the tropical atmosphere, although some studies suggest that there may not be a relation between CAPE and triggering of convection (Mapes, 2000; Mapes & Houze, 1992). In the original SMCM, convective available energy (denoted C) integrated over the whole troposphere is used in combination with midlevel moisture or rather dryness, denoted D. Since, in general, deep convective clouds involve free buoyant ascent air, CAPE is used as the first large-scale predictor:

$$x_{CAPE} = \frac{CAPE}{CAPE0}, \tag{1}$$

where $CAPE0$ represents a scaling factor. In Khouider et al. (2010), dryness is calculated as the fraction of difference between the equivalent potential temperature in the midtroposphere and the boundary layer, $\theta_{eb} - \theta_{em}$, and a climatological scaling factor of $15K$. In our study, we follow Peters et al. (2013) and define the dryness D with respect to the relative humidity at 500 hPa expressed through

$$x_D = 2(1 - RH_{500}). \tag{2}$$

The same approach was adopted in Goswami et al. (2017a, 2017b, 2017c). High values of relative humidity at 500 hPa are considered favorable for deep convection. In fact, Johnson and Lin (1997) found a positive correlation between tropospheric humidity and organized tropical convection. The existence of moisture above the boundary layer over warm tropical oceans seems to stimulate convective development more than CAPE in the tropical Pacific. Interestingly, moisture in the lower layers is also considered a good indicator for convection (Sherwood, 1999). The combination of low dryness values together with high values of CAPE represent favorable conditions for deep convective events. On the other hand, high values of CAPE in a dry atmosphere create good conditions for the formation of congestus clouds (Khouider & Majda, 2006b); moist parcels rising in a dry environment tend to quickly lose buoyancy and detrain in the midtroposphere. In Khouider et al. (2010), a new form of CAPE, called low-level CAPE, obtained by integrating positive buoyancy of a hypothetical rising parcel until the freezing level—set roughly in the midtroposphere—is used as an indicator for congestus clouds. Following De La Chevrotière et al. (2014), a rescaled low-level CAPE is used as a predictor for congestus clouds:

$$x_{LCAPE} = \frac{CAPE_l}{CAPE0}. \tag{3}$$

The first of the three new predictors introduced in this study is CIN, which corresponds to the energy that an air parcel has to overcome in order to continue its upward motion and reach its level of free convection. We scale CIN in the same way as CAPE and low-level CAPE:

$$x_{CIN} = \frac{CIN}{CIN0}. \tag{4}$$

The next predictor is a measure of the trade wind inversion. The vertical gradient of virtual potential temperature θ_v is informative of the static stability of the atmosphere. A decrease of θ_v with height indicates a statically unstable atmosphere, an increase corresponds to static stability, and a constant virtual potential temperature reflects neutral conditions. It is known that the trade wind inversion in the tropics originates from the interaction between large-scale subsiding air from the upper troposphere and convection-driven rising air from lower levels. Thus, convection-driven air can raise the inversion layer (Emanuel & Raymond, 1993). The gradient of θ_v is also proportional to the buoyancy frequency for unsaturated moist air. We capture the highest value of θ_v gradient in the layers $0 \le z \le z_l$ ($z_l = 4$ km) and scale it with a reference stratification T_z:

$$x_{Inv} = \frac{1}{T_z} \max\left(\frac{\mathrm{d}\theta_v}{\mathrm{d}z}\right). \tag{5}$$

Moreover, it is well known that vertical velocity is intimately related to convection on all scales (Donner, 1993; Kain & Fritsch, 1990). We are particularly interested in the instance when large-scale subsidence enforces the inversion layer and inhibits deep penetrative convection. Due to the coarse resolution used in climate models, it is very likely that the actual trade wind inversion is not resolved or well simulated, the same can be true for CIN. We thus reinforce the last two predictors with a measure of large-scale subsidence:

$$x_{w^-} = -\frac{1}{W_0} \max(0, -w), \tag{6}$$

where the maximum is taking over all vertical layers between 500 and 4,000 m. Combined together, the last three indicators are chosen to provide a comprehensive threshold for penetrative convection, beyond which congestus and deep convection are allowed to develop. This is in contrast with Peters et al. (2013) who used positive large-scale vertical velocity at 500 hPa as a predictor for convection instead of CAPE. The use of *CIN*, the strength of the low-level trade inversion, and large-scale subsidence to inhibit deep convective and congestus clouds and promote shallow cumulus may seem like an overkill since the three are all connected, but, once again, CIN and the inversion layer can be underresolved by the GCM vertical grid, so some redundancy is warranted.

The quantities $x_{CAPE}, x_D, x_{LCAPE}, x_{CIN}, x_{Inv}$, and x_{w-} constitute the large-scale predictors that are used by the extended SMCM to simulate the dynamical evolution and interactions of the three cloud types—congestus, deep convective, and stratiform—between each other and the given large-scale conditions of the atmosphere. We note the rescaling constants $\mathrm{CAPE}_0 = 1,000$ J/kg, $\mathrm{CIN}_0 = 5$ J/kg, $T_z = 4$ K/km, and $W_0 = 1$ m/s

Table 1
Transition Rates R^i_{kl}, $(k, l = 0, 1, 2, 3)$ *Expressed in Terms of* $\Gamma(x)$ *Where* $x_{predictor} = (x_{CAPE}, x_{LCAPE}, x_D, x_{CIN}, x_{\omega^-}, x_{Inv})$

Transition type	Transition rate equations
Congestus to deep	$R_{12} = \frac{1}{\tau_{23}}\Gamma(x_{CAPE})(1-\Gamma(x_D))[1-(\Gamma(x_{CIN})\Gamma(x_{\omega^-})\Gamma(x_{Inv})]$
Deep to stratiform	$R_{23} = \frac{1}{\tau_{23}}$
Decay of congestus	$R_{10} = \frac{1}{\tau_{10}}$
Decay of deep	$R_{20} = \frac{1}{\tau_{20}}$
Decay of stratiform	$R_{30} = \frac{1}{\tau_{30}}$
Formation of congestus	$R_{01} = \frac{1}{\tau_{01}}\Gamma(x_{LCAPE})\Gamma(x_D)[1-\Gamma(x_{CIN})\Gamma(x_{\omega^-})\Gamma(x_{Inv})]$
Formation of deep	$R_{02} = \frac{1}{\tau_{02}}\Gamma(x_{CAPE})(1-\Gamma(x_D)[1-\Gamma(x_{CIN})\Gamma(x_{\omega^-})\Gamma(x_{Inv})]$

Note. The corresponding τ_{kl} are the time scale parameters.

are chosen so that the rescaled predictors, $x_{\cdot}$, in (1)–(6), take values roughly between 0 and 2, on average, in order to accommodate the Arhenius-type triggering function, Γ, which defines the probabilistic transition rates, in terms of the large-scale indicators, that are summarized in Table 1:

$$\Gamma(x) = \begin{cases} 1 - e^{-x} & \text{if} \quad x > 0 \\ 0 & \text{otherwise.} \end{cases} \tag{7}$$

Nonetheless, it is worthwhile noting that the results can be sensitive to the choice of those normalizing constants. Devising the best strategy on how to choose these constants is not a simple matter. We return to this issue in section 5.

Listed below are the assumptions on which the SMCM transition rates used in this work are based. As already mentioned, these rules may apply only to organized convection over the ocean. Extensions of the SMCM framework to midlatitude or continental convection are possible through the inclusion of the background shear and other large-scale variables. This can be achieved by using instead the SMCM model with local interaction introduced in Khouider (2014). Also, an SMCM version for costal convection in the Maritime Continent taking into account the sea-breeze effect is introduced and used in Bergemann et al. (2017).

1. Following Khouider et al. (2010), it is assumed that on the infinitesimal time scale, it is not likely for a clear site or congestus site to turn into a stratiform site. There is no indication from observations that deep convective or stratiform clouds might convert to congestus clouds or that stratiform clouds can convert to a deep convective clouds (same assumption as in the original SMSM). Thus, $R_{03} = R_{13} = R_{21} = R_{31} = R_{32} = 0$.
2. A clear sky site turns into a congestus site if there is high low-level CAPE and the middle troposphere is dry.
3. A congestus or clear site turns into a deep site with high probability if *CAPE* is positive, the middle troposphere is moist and *CIN*, *Inv* are weak or not present, and x_{w^-} is nonpositive.
4. A clear sky site turns into a congestus site if low-level *CAPE* is positive, the middle troposphere is dry, *CIN* and *Inv* are weakly positive or not present, and x_{w^-} is negative.
5. A deep convective site turns into a stratiform site with a constant conversion rate.
6. A site occupied by one of the clouds turns into a clear sky site with a constant decay time scale, independent of the large-scale predictors, for each one of the clouds.

This defines a continuous-time Markov chain process, X^i_t $(i = 1 \ldots N, t = t_1 \ldots t_T)$, that takes one of the four values, 0,1,2,3, according to whether, at time t, the corresponding lattice site is occupied by one of the cloud

sites or it is a clear sky site.

$$X_t^i = \begin{cases} 0, \text{ if site } i \text{ is clear sky,} \\ 1, \text{ if site } i \text{ is occupied by congestus,} \\ 2, \text{ if site } i \text{ is occupied by deep convective,} \\ 3, \text{ if site } i \text{ is occupied by stratiform.} \end{cases}$$

The total number of lattice sites occupied by congestus, deep convective, stratiform, and clear sky, at time t, within a GCM grid box,

$$N_c^t = \sum_{i=1}^{N} 1\left(X_t^i = 1\right), N_d^t = \sum_{i=1}^{N} 1\left(X_t^i = 2\right), N_{cs}^t = \sum_{i=4}^{N} 1\left(X_t^i = 3\right), N_{cs}^t = N - N_c^t - N_d^t - N_s^t,$$

is used to compute the area fraction associated with each cloud type, or clear sky, by simply dividing by the total number of lattice sites, N, in that region or grid box:

$$\sigma_c^t = \frac{N_c^t}{N}, \sigma_d^t = \frac{N_d^t}{N}, \sigma_s^t = \frac{N_s^t}{N}, \sigma_{cs}^t = 1 - \sigma_c - \sigma_d - \sigma_s.$$

At a later time $t+dt$, where dt corresponds to an infinitesimal time step, the process X_t^i will make a transition from a given state to another, according to the conditional probabilities:

$$P_{kl}^i = P(X_{t+\Delta t}^i = l / X_t^i = k) = R_{kl} dt + o(dt), \text{if} \quad k \neq lk, l = 0, 1, 2, 3, \tag{8}$$

$$P_{kk}^i = P(X_{t+\Delta t}^i = k / X_t^i = k) = 1 - \sum_{l=1, l\neq k}^{3} R_{kl}^i dt + o(dt), \; k = 0, 1, 2, 3. \tag{9}$$

The transition rates R_{kl} are given in Table 1 and depend exclusively on the suite of large-scale predictors described above through the Arhenius-type function Γ modulated by the transition rates, τ_{kl}, which we aim to infer from data. It is important to note that by design, these transition rates are formulated so that the stochastic process, X_t^i, forms an ergodic Markov Chain at each lattice site, i, with the same invariant distribution depending solely on the large-scale predictors and the transition time scales, τ_{kl}, and whose values can be interpreted as the expected or the climatological mean area fractions of the three cloud types in the given GCM box. By design, the transition rates were constructed so that the Markov chain obeys detailed balance with respect to this stationary distribution, thus guaranteeing convergence to equilibrium in the long run. Peters et al. (2013) compared the dependence of this equilibrium distribution on the large-scale predictors and observed cloud area fractions to tune the transition time scales. In the more complex case, when the transition rates depend on local interactions between neighboring sites, the design principle is to assume that the equilibrium distribution is the grand canonical Gibbs measure of statistical mechanics and transition rates are based on the Metropolis dynamics for Markov Chain Monte Carlo (MCMC) sampling of this measure (Khouider, 2014).

Following Khouider et al. (2010), the bulk cloud type numbers within the GCM box—N_c, N_d and N_s—form a multidimensional birth-death stochastic process obeying the "coarse-grained" transition probabilities. The probabilities are obtained by summing up the possibilities for any given bulk change in each one of these numbers, over all lattice sites within the GCM box. The probability for the birth of a single congestus site, for instance, over an infinitesimal time, dt, is given by

$$P\{N_c^{t+dt} = k + 1 | N_c^t = k\} = N_{sc}^t R_{01} dt + o(dt), \tag{10}$$

which is simply the rate of transition from clear sky to congestus multiplied by the total number of clear sky sites that are available, while the probability of death is given by

$$P\{N_c^{t+dt} = k - 1 | N_c^t = k\} = N_c^t (R_{10} + R_{12}) dt + o(dt), \tag{11}$$

with the similar obvious interpretation. More details are found in Khouider et al. (2010). We thus obtain the infinitesimal transition probabilities (and rates) of a birth-death process defining the stochastic evolution

of N_c, N_d, and N_s. The coarse-graining procedure allows an efficient simulation of these quantities without dealing with the microscopic lattice configurations.

According to the theory of Markov chains, the expressions of the transition probabilities represented by equations (10) and (11) are approximately valid for a finite time step dt, as long as the latter is sufficiently small. As such they can, for instance, be used to simulate the birth-death process when the transition rates are known. However, the Bayesian procedure requires the evaluation of the transition probabilities at time intervals that are limited by the resolution of the radar observations of the actual congestus, deep convective, and stratiform rain areas (in this case, 10 min) that are used to infer the unknown time scales, τ_{kl}, which appear in front of the transition rates in Table 1. Instead, the algorithm used here relies on an accurate approximation of the solution to the Kolmogorov backward equations (De La Chevrotière et al., 2014) for the coarse-grained multidimensional birth-death process, which govern the probabilistic evolution in time of the bulk cloud numbers, N_c, N_d, N_s, or equivalently the area fractions, $\sigma_c, \sigma_d, \sigma_s$. In particular, the Bayesian methodology applied directly to the coarse-grained birth-death process requires only the knowledge of the cloud area fractions within the GCM grid box of interest. An overview of the Bayesian procedure is presented in the next subsection. More details are found in De La Chevrotière et al. (2014).

2.3. The Bayesian Parameter Inference Approach

Let $\boldsymbol{y}^t_{\mathbf{cloud}} = (N^t_c, N^t_d, N^t_s)$ be the time-dependent vector of the numbers of lattice sites (pixels) occupied by the associated three cloud types and

$$\boldsymbol{x}^t_{\mathbf{predictor}} = (x_{CAPE}, x_{LCAPE}, x_{CIN}, x_D, x_{Inv}, x_{w^-})$$

the corresponding large-scale predictors that are obtained from the sounding observations. The SMCM assumes a probabilistic relation between these two variable vectors, which can be written in abstract form as

$$\boldsymbol{y}^t_{\mathbf{cloud}} = F\left(\boldsymbol{\Phi}, \boldsymbol{x}^t_{\text{predictor}}\right). \tag{12}$$

Here is the vector of *unknown parameters of interest*, representing the transition time scales to be inferred from the radar data:

$$\boldsymbol{\Phi} = (\tau_{01}, \tau_{10}, \tau_{12}, \tau_{02}, \tau_{23}, \tau_{20}, \tau_{30}). \tag{13}$$

Precisely, we have data derived from measurable variables, and we intend to find a different type of quantities (the transition time scales) using a suitable method. This can be viewed as an *inverse problem*. To take into account the uncertain nature of the parameters in $\boldsymbol{\Phi}$, we opt for a probabilistic method based on Bayesian inference. Given the observations, contained in the vector $\boldsymbol{y}^t_{\text{cloud}}$, the Bayesian inference method (De La Chevrotière et al., 2016) finds the conditional distribution of Φ, $p_{\text{posterior}}(\boldsymbol{\Phi}|\boldsymbol{y}^t_{\text{cloud}})$, in terms of the known conditional probability distribution of the observations, $f(\boldsymbol{y}^t_{\text{cloud}}|\boldsymbol{\Phi})$, known as the *likelihood function* and a prior distribution, $p_{\text{prior}}(\boldsymbol{\Phi})$, of the parameters. The prior distribution is user defined and can take an arbitrary form, and as such, it can take into account any prior knowledge about the parameters. As formulated, the posterior distribution depends directly on the choice of the prior distribution. However, as shown in De La Chevrotière et al. (2014), as the observed data set becomes larger, the limiting posterior distribution seems to be insensitive to whether the prior is uniform or Gaussian distributed. Starting with Bayes' Theorem,

$$p_{\text{posterior}}(\boldsymbol{\Phi}|\boldsymbol{y}^t_{\text{cloud}}) = \frac{f(\boldsymbol{y}^t_{\text{cloud}}|\boldsymbol{\Phi})p(\boldsymbol{\Phi})}{prob(\boldsymbol{y}^t_{\text{cloud}})}, \quad prob(\boldsymbol{y}^t_{\text{cloud}}) = \int prob(\boldsymbol{y}^t_{\text{cloud}}|\boldsymbol{\Phi})p_{\text{prior}}(\boldsymbol{\Phi})\mathrm{d}\boldsymbol{\Phi}, \tag{14}$$

we insert the dependence on the predictors vector x_t

$$p_{\text{posterior}}(\boldsymbol{\Phi}|\boldsymbol{y}^t_{\text{cloud}}, \boldsymbol{x}^t_{\text{predictor}}) \propto f(\boldsymbol{y}^t_{\text{cloud}}|\boldsymbol{x}^t_{\text{predictor}}, \boldsymbol{\Phi})p_{\text{prior}}(\boldsymbol{\Phi}). \tag{15}$$

Since the initial prior distribution is updated at each time step, as more information becomes available, we can write the stepwise model likelihood function taking advantage of the fact that it is the probability distribution of a Markov process:

$$f(\boldsymbol{y}^{1:T}_{\text{cloud}}|\boldsymbol{x}^{1:T}_{\text{predictor}}, \boldsymbol{\Phi}) = \prod_{t=1}^{T} f^{t-1}\left(\boldsymbol{y}^t_{\text{cloud}}|\boldsymbol{y}^{t-1}_{\text{cloud}}, \boldsymbol{x}^{t-1}_{\text{predictor}}, \boldsymbol{\Phi}\right), \tag{16}$$

where $\boldsymbol{y}_{\text{cloud}}^{1:T}$ and $\boldsymbol{x}_{\text{predictor}}^{1:T}$ are the series of observations of a given length T, corresponding to clouds and predictors, respectively.

The transition probability matrix of the time-continuous Markov chain process associated with the birth-death cloud model solves a system of differential equations known as the Kolmogorov backward equations. In matrix notation,

$$P'^{(t)} = R\left(\boldsymbol{x}_{\text{predictor}}^{t}, \boldsymbol{\Phi}\right) P(t). \tag{17}$$

Here $P'^{(t)}$ is the time derivative of the probability function, and R is the transition rates matrix (a.k.a the infinitesimal generator) given as a function of the large-scale predictors and the parameters vector $\boldsymbol{\Phi}$ (Table 1). For constant $\boldsymbol{x}_{\text{predictor}}^{t}$ and constant $\boldsymbol{\Phi}$ vectors, the general solution of this system is given by

$$P(t) = \exp[R(\boldsymbol{x}_{\text{predictor}}^{t}, \boldsymbol{\Phi})(t - t_0)]P(t_0). \tag{18}$$

Thus, assuming that the predictor vector is constant between successive observations, the computation of the stepwise transition model likelihood function becomes the problem of evaluating $T-1$ matrix exponentials, for a sample of size T. Here we apply this procedure to three different samples of sizes $T = 144$, $T = 269$, and $T = 477$. The size of the exponential matrix depends on the size of the lattice model. Having a lattice model of size N, the Markov chain process evolves over time on a finite space $S \subset \mathbb{N}^3$, a set of ordered triplets of positive integers (z_1, z_2, z_3) such that

$$z_1 + z_2 + z_3 \leq N = n \times n.$$

Here we set $n = 10$ or $N = 100$. Let θ be a mapping of each triplet to a counting order

$$\theta : S \to \mathbb{N},$$

and let $z_1 = N_c^t, z_2 = N_d^t, z_3 = N_s^t$, then we have (De La Chevrotière et al., 2014)

$$f\left(\boldsymbol{y}_{\text{cloud}}^{1:T} | \boldsymbol{x}_{\text{predictor}}^{1:T}, \boldsymbol{\Phi}\right) = \prod_{t=1}^{T} 1_{\theta\left(N_c^{t-1}, N_d^{t-1}, N_s^{t-1}\right)} \exp\left[R\left(\boldsymbol{x}_{\text{predictor}}^{t}, \boldsymbol{\Phi}\right) h\right] 1_{\theta\left(N_c^{t-1}, N_d^{t-1}, N_s^{t-1}\right)}. \tag{19}$$

To solve the large sparse matrix exponentials, a uniformization method based on the partial Taylor series extension combined with a preconditioner to avoid the proliferation of roundoff errors is used. This uniformization method is implemented using the PETSc library for a fast computation of the large matrix-vector products. The MCMC method, based on Gibbs Sampling, is then used to obtain reliable statistics of the posterior distribution in (15) to overcome the unavailability of a closed form solution (De La Chevrotière et al., 2014). Further details on this procedure are described in De La Chevrotière et al. (2014).

3. DYNAMO Data Sets and Case Studies

3.1. DYNAMO and the MJO

The DYNAMO field campaign was conducted from October 2011 to March 2012 in the equatorial Indian Ocean to better understand the mechanisms related to moistening of the troposphere and the role of clouds as well the impact of the interaction of air and sea in the initiation phase of the MJO (Yoneyama et al., 2013). The MJO is a dominant atmospheric disturbance on the intraseasonal scale, at the intersection of weather and climate variability, which initiates over the central Indian Ocean as a planetary-scale coherent envelope of winds and convection (Zhang, 2005, 2013; Zhang et al., 2013). The MJO propagates along the equator at roughly 5 m/s over the Maritime Continent, and its convection typically dies before it reaches the Central Pacific. It impacts both midlatitude and tropical weather and climate variability, such as the development and frequency of tropical cyclones (Klotzbach & Oliver, 2014; Liebmann et al., 1994), the rainfall variability in different regions of the globe (Hendon & Liebmann, 1990; Lawrence & Webster, 2002), and seasonal variations of the El Niño-Southern Oscillation (Hendon et al., 2007).

The MJO is also characterized by the presence of repetitive cloud structures and precipitation patterns; in particular, some studies have shown that during its active phase, convection transitions from shallow cumulus to cumulus congestus, which evolve to deep convective clouds and then to stratiform anvils (Benedict

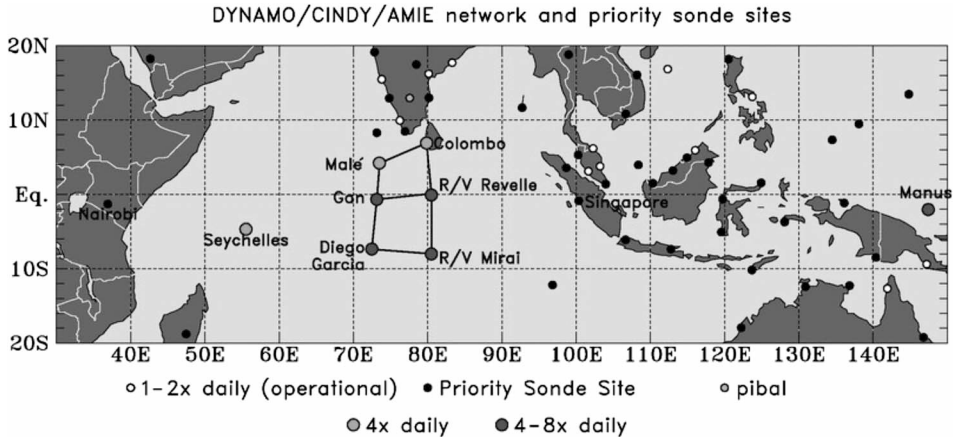

Figure 2. Location of the upper-air sounding network, the DYNAMO/CINDY/AMIE polygons. The Northern Sounding Array comprises the boundary sites Colombo, Revelle, Gan, and Male. The Southern Sounding Array is defined by Revelle, Mirai, Diega Garcia, and Gan. DYNAMO = Dynamics and the Madden-Julian Oscillation; CINDY = Cooperative Indian Ocean Experiment on Instraseasonal Variability; AMIE = Atmospheric Radiation Measurement Madden-Julian Oscillation Investigation Experiment. Source: http://johnson.atmos.colostate.edu/dynamo/products/array_averages/index.html/.

& Randall, 2007; Haertel et al., 2008; Johnson et al., 1999; Kikuchi & Takayabu, 2004; Morita et al., 2006). Despite continued efforts and improvements in climate models, the initiation and propagation of the MJO are still not well simulated (Henderson et al., 2017; Hung et al., 2013; Khouider et al., 2013; Lin et al., 2006). It is assumed that the poor representation of clouds, the interaction between clouds (Crueger & Stevens, 2015), and radiation and moisture contribute to the inability of GCMs to simulate the MJO.

For this study, we use two separate DYNAMO data sets for the quantification of the large-scale predictors and the cloud area fractions time series. Both are spatially averaged over a mesoscale area corresponding roughly to a GCM grid box, consistent with the design of the SMCM (Khouider et al., 2010). This averaging will likely introduce some errors in the predictors, especially given the sparseness of the DYNAMO sounding network. Although close inspection showed that the predictors are close to ERA Interim data (results not shown), a sensitivity study to the predictors is desirable and will be conducted and reported elsewhere by the authors. More importantly, the inference strategy done here, in a "freestanding" mode where only the cloud area fractions are simulated, is somewhat idealistic. The strategy used here assumes perfect knowledge of the large-scale predictors and does not take into account the associated model error when the SMCM is coupled to a GMC. Because of the intrinsic two-way coupling between large-scale dynamics and convection, especially in the case of the MJO, it is desirable to have a likelihood function that takes into account the coupled MJO-convection system as a whole. However, this would require a full GCM, or at least a regional climate model, coupled to the SMCM. While such a model is highly desirable, it will make the computation of such likelihood function prohibitive. To overcome such difficulty, Järvinen et al. (2012) incorporated the Bayesian framework into an existing forecast system to estimate parameters associated with subgrid parameterizations in the ECHAM5 model. Such strategy is not feasible at the moment for the SMCM since it is not yet integrated into an operational model. In principle, it is conceivable to consider such a two-way coupled likelihood model with a single-column model to represent the dynamics of the environmental variables as in Khouider et al. (2010), for example, but it remains to explicitly compute the probability distribution of the coupled dynamical system. Nonetheless, transition parameters inferred using the same strategy, as the one used here, that is, of assuming perfect knowledge of the large-scale dynamics (De La Chevrotière et al., 2016), have been successfully used in Goswami et al. (2017a, 2017b, 2017c) to improve the simulation of the MJO and other tropical modes of variability.

3.2. DYNAMO Data for the Predictors

The sounding-array averaged data from the DYNAMO field campaign (Johnson & Ciesielski, 2013) is used to compute the large-scale predictors of convection. The sounding-array observations were processed using a multiquadric interpolation scheme from Nuss and Titley (1994), onto a regular 1° and 25-hPa grid. The resulting data set comprises a north and a south quadrilateral array: NSA and SSA. The NSA and SSA

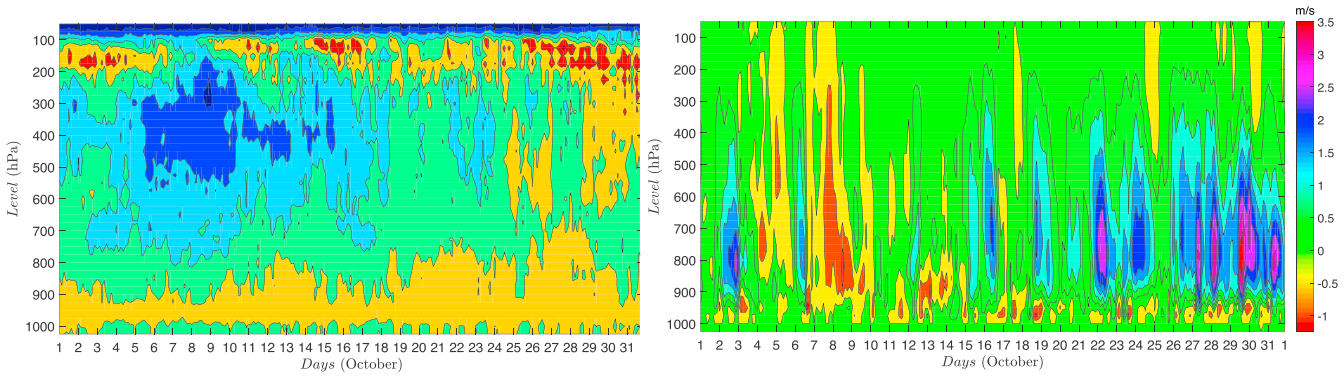

Figure 3. Time-height structure of averaged relative humidity (in % with respect to ice for $T < 0$, left), and vertical velocity (right) averaged over the Northern Sounding Array and the Southern Sounding Array from the 1st till 31st of October.

are a split between the northern and southern parts of an intensive observation region located in the central-equatorial Indian Ocean, around the Maldives, between roughly 7°S–8°N and 72–80°E, as depicted in Figure 2. The sounding array is comprised by a total of six observation stations, four over surrounding islands and the two others use stationary research ships, each collecting data between 4 and 8 times a day.

This array type presents an improvement in terms of budget computations when compared with the previous triangular arrays of the Mirai Indian Ocean Cruise for the Study of the MJO Onset (Katsumata et al., 2011) and offers a higher temporal resolution of 3 hr (00, 03, 06, 09, 12, 15, 18, and 21 UTC) in contrast to the 6-hourly sounding data obtained in the Tropical Ocean Global Atmosphere Coupled Atmosphere-Ocean Response Experiment (Ciesielski et al., 2003; Webster & Lukas, 1992). It is expected that the DYNAMO sounding observations capture the necessary information to describe the real state of the atmosphere in order to simulate the birth and death process of clouds over the Indian Ocean, especially during the initial phase of the MJO. The basic available meteorological variables are geopotential height (z), zonal wind (u), meridional wind (v), surface pressure (p_s), vertical pressure velocity (ω), temperature (T), potential temperature θ, water vapor mixing ration (wmr), relative humidity (rh), divergence (div), and relative vorticity (ξ). In our study, only the thermodynamic variables, T, θ, q, and one dynamical variable, namely, ω (converted to vertical velocity w), are used to compute the convection predictors, specified above.

The DYNAMO experiment witnessed the occurrence of three MJO events between October 2011 and January 2012 (Gottschalck et al., 2013), one in October, one in November, and one between late December and early January. The time-height contours of NSA+SSA averaged relative humidity and vertical velocity during the month of October are shown in Figure 3. The two panels depict two distinct phases of the October MJO: a preinitiation period characterized by a dry upper troposphere and large-scale subsidence prior to 16 October, which is known to be the MJO initiation date (at least over the NSA-SSA arrays), and after 16 October, which is characterized by a moist upper troposphere and narrowly successive coherent periods of intense upward motion. The two periods correspond to the suppressed and active phases of the MJO, respectively.

3.3. SMART-R Rain Types

The second data set, used for the cloud area fractions, is from SMART-R, a scanning Doppler C-band radar that was on Addu Atoll during DYNAMO (Fliegel, 2011). SMART-R was deployed to obtain a continuous (every 10 min), three-dimensional view of the precipitating clouds during each phase of the MJO. SMART-R data were interpolated at 2-km horizontal and 0.5-km vertical resolution out to a 150-km radius from the radar. Because of tree blockage to the west, low-level scans were blocked in that direction so only a 180° sector to the east is used in this analysis. We also limit our analysis to 100 km from the radar to mitigate the impact of beam spreading and so forth on the rain type classifications. This data set is available from 2 October 2011 to 9 February 2012.

The SMART-R reflectivity data were first separated into convective and stratiform rain types using the horizontal texture method of Steiner et al. (1995). The rain types were then modified using echo-top heights and an isolation parameter to reclassify isolated echo with echo tops <9 km as convective rather than stratiform (Fliegel, 2011). The final step was to separate the convective rain into congestus and deep categories using an echo-top threshold of 7 km. Feng et al. (2014) showed that SMART-R had very similar mean frequencies

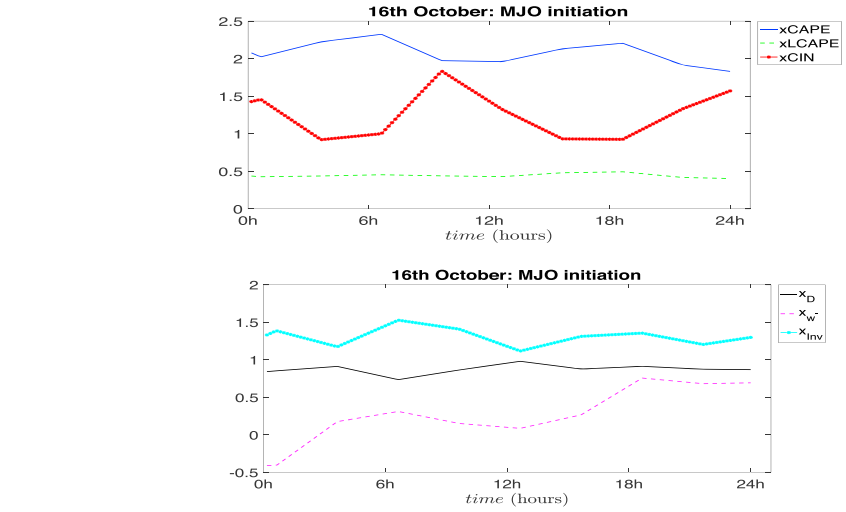

(A)

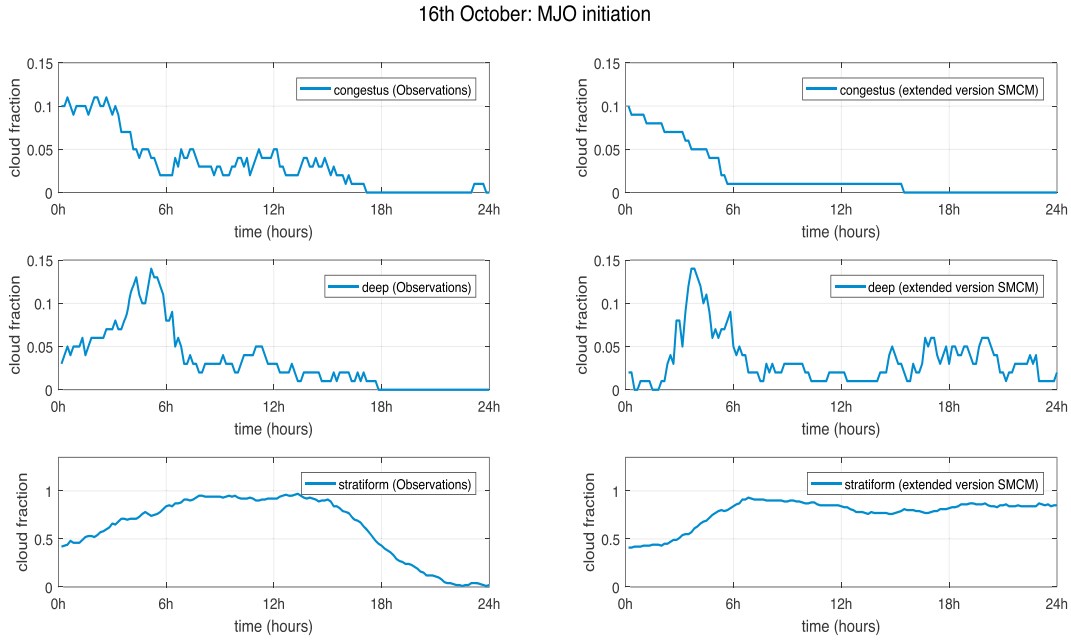

(B)

Figure 4. (a) Time series of the normalized large-scale predictors (October 16 [$T = 144$]; see text for details) obtained from interpolating in time to 10-min resolution, the averaged combination of Northern Sounding Array and Southern Sounding Array sounding arrays from Dynamics and the Madden-Julian Oscillation, meteorological variables, to test the Bayesian procedure. (top) CAPE, Low-level CAPE, and CIN. (bottom) Dryness, vertical velocity, and inversion maximum. (b, left) Cloud fraction time series plots for the Shared Mobile Atmospheric Research and Teaching Radar congestus, deep, and stratiform cloud area fractions for the 1-day period test case corresponding to the Madden-Julian Oscillation initiation of 16 October. (right) Same as left but for the stand-alone extended SMCM simulated cloud fractions using the corresponding observed Dynamics and the Madden-Julian Oscillation predictors and the corresponding inferred transition time scales (see section 4.2). SMCM = stochastic multicloud model.

of congestus and deep convective clouds compared to radars with other wavelengths and scanning strategies during DYNAMO. The areas of each of the three precipitating cloud types (congestus, deep convective, and stratiform) were then calculated every 10 min over the radar domain to create cloud area fraction time series. The resulting time series are used within the Bayesian framework as the observed variable $\boldsymbol{y}^t_{\text{cloud}}$, according to equation (15). To match the time resolution of the area fraction time series obtained from SMART-R,

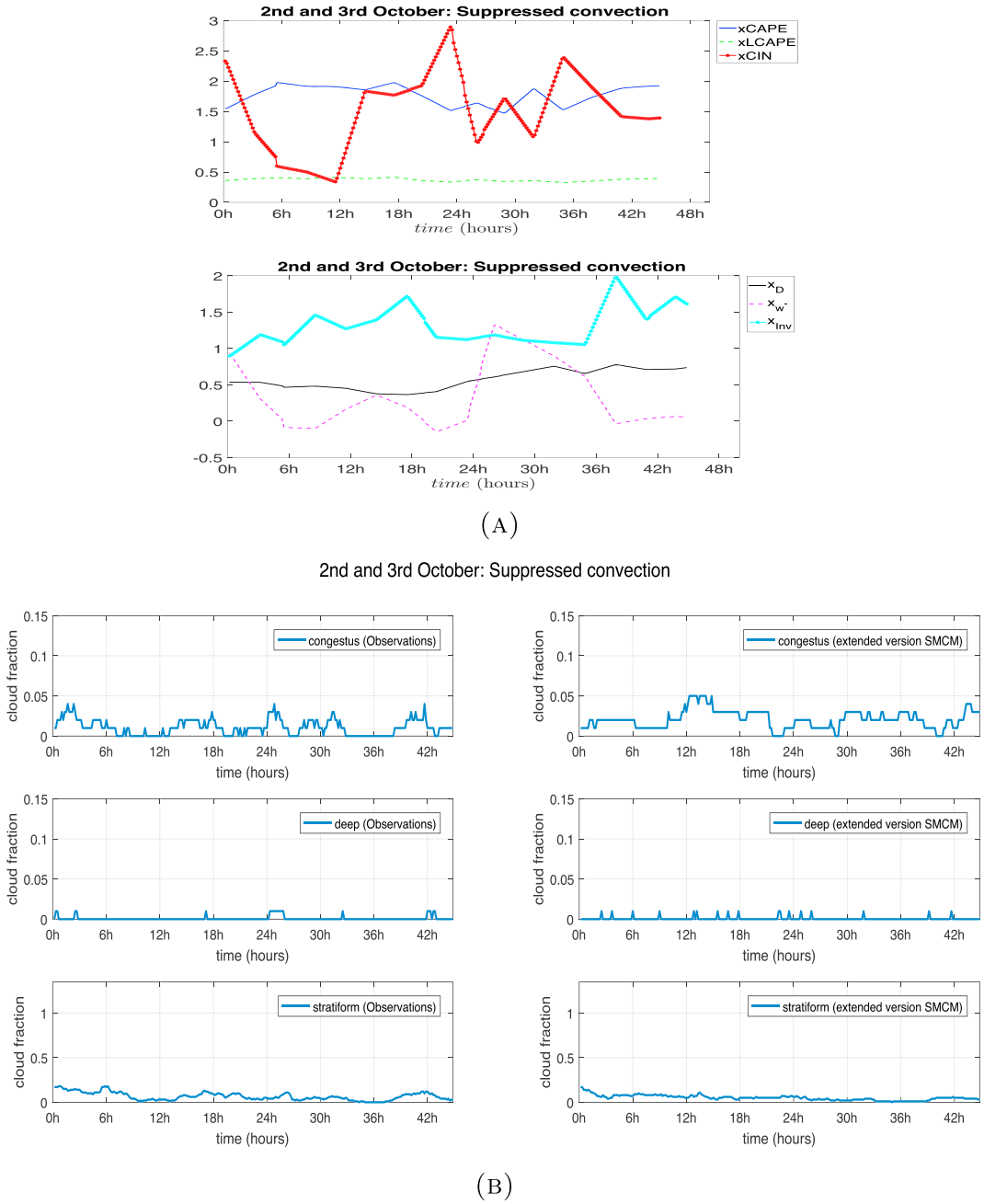

Figure 5. Same as in Figure 4 but the case of a 2-day period subset extending between 2 and 3 October ($T = 269$), during the suppressed Madden-Julian Oscillation phase.

the large-scale predictors were computed from the NSA-SSA 3-hourly average DYNAMO meteorological variables and then interpolated linearly into a 10-min continuous record.

3.4. Three Reference Test Cases

An important drawback of the Bayesian inference used here is, as for all data-intensive methods, its use of large computational resources. Recall that for a data set (cloud-predictor couplet) of size T, the method requires the computation of $T - 1$ large matrix exponentials to generate one sample of the MCMC algorithm and that thousands of samples are typically needed to reach convergence of the MCMC chains (De La Chevrotière et al., 2014, 2016). Thus, in order to provide an efficient preliminary testing environment for the SMCM-Bayesian model using real data, we chose three relatively small samples from the two DYNAMO data sets described above with sizes varying between 1 and roughly 3 days. Specifically, we consider a 1-day period

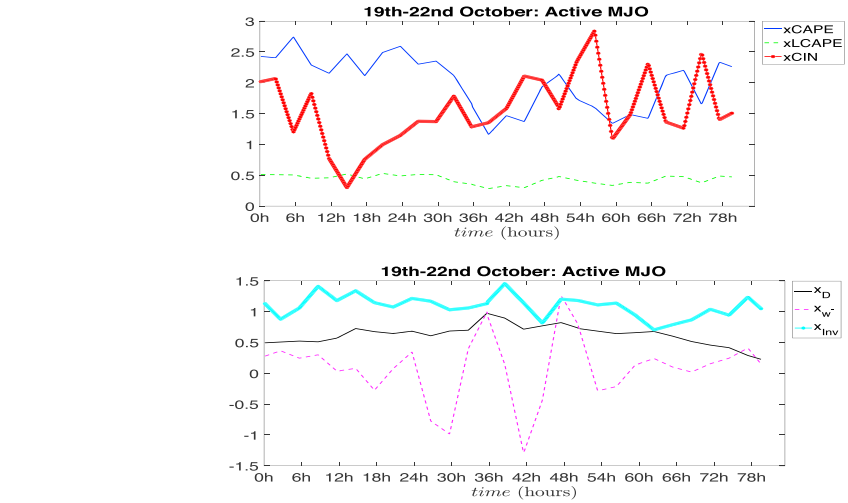

(A)

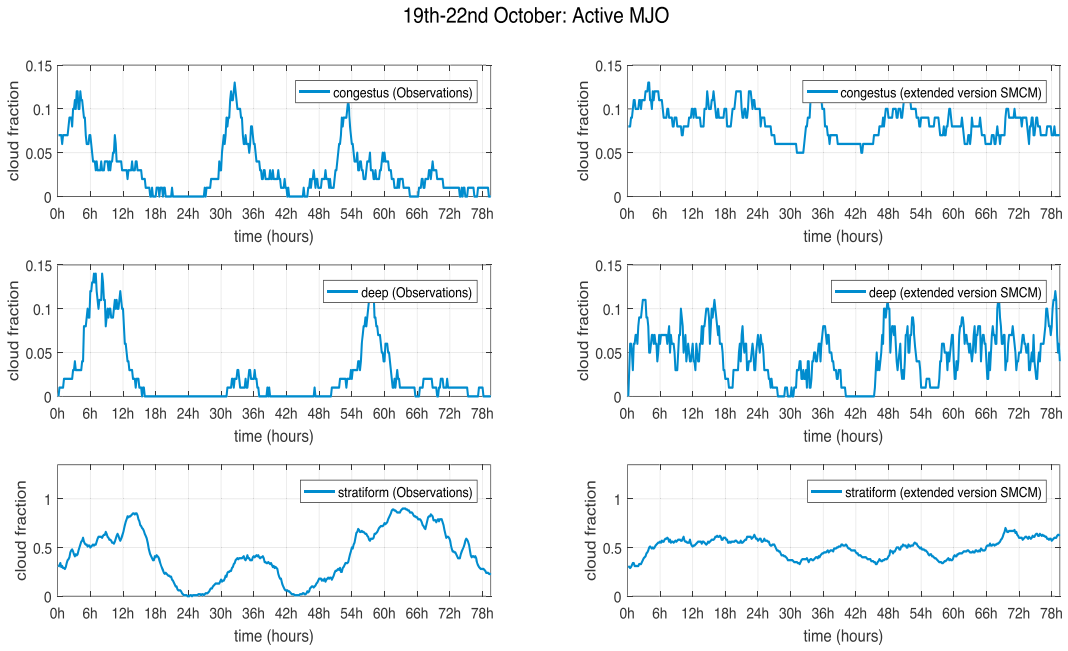

(B)

Figure 6. Same as in Figure 4 but the case of a 4-day period subset extending between 19 and 22 October ($T = 477$), during the active Madden-Julian Oscillation phase.

corresponding to the initiation of the MJO (16 October), a 2-day period during the MJO suppressed phase (2–3 October), and a 3-day period within the active phase (19–22 October). With the fixed time step of 10 min, the three subsets correspond to three time series of cloud-predictor couplets of sizes $T = 144$, $T = 269$, and $T = 477$, respectively.

The varying lengths of the training periods may seem arbitrary but is actually motivated under the constraint of computing resources. The periods chosen are a compromise between using something meaningful and practical. For the meaningful part, our strategy is based on a combination of the experience from De La Chevrotière et al. (2016) and the physics of the problem. De La Chevrotière et al. (2016) used a 1-day long LES run that was transformed into a 2-day long and a 4-day long time series by dividing the computational domain into 2 and 4, respectively. Thus, having time series in the bulk part of 1 to 4 days is deemed appropriate. Also, the MJO initiation phase is generally very short, so we use 1 day only for that experiment, while we

somewhat arbitrarily choose 2 days for the suppressed phase and 3 days for the active phase. Nonetheless, the computation resources required are still enormous. Combined with the fact that the MCMC chains were monitored externally and we used an overly conservative convergence criterion, it took 4 weeks to complete the $T = 144$ test case, 8 weeks for the $T = 269$ case, and 12 weeks for the $T = 477$ case. For each case, we used 72 cores in parallel on a linux cluster.

The interpolated large-scale predictors *CAPE*, *LCAPE*, *D*, *CIN*, w^-, and *Inv* computed from the DYNAMO data for the three selected time samples are plotted in Figures 4–6, while the aggregated SMART-R congestus, deep convective, and stratiform area fractions are reported on the right panels of Figures 4–6, respectively. We now describe the meteorological conditions associated with each one of the three testing periods in terms of these large-scale predictors and how they relate to the SMART-R area fraction time series. This is helpful in order to understand the physical significance of those predictors in the context of the SMCM.

3.4.1. 16 October: MJO Initiation

The large-scale conditions for the 16 October 2011, as presented on Figure 4, are characterized by two peaks of roughly 2,300 and 2,200 J/kg in *CAPE* (according to the normalizing value of $CAPE_0 = 1{,}000$ J/kg) at slightly past 6 am and 6 pm, respectively. They are matched by the same number of corresponding peaks in *LCAPE*—although weak—of 450 and 490 J/kg (and almost undistinguishable on the plots). CIN, on the other hand, first decreases to reach a minimum of roughly 8 J/kg ($CIN_0 = 5$ J/kg) about 2 hr before 6 am and then picks up sharply after and peaks at about 10 am, reaching a maximum of 18 J/kg. It then plunges down to reach a second minimum around 6 pm. Though not exactly in phase, the two minima in CIN coincide with the two maxima in *CAPE* and *LCAPE*.

Dryness at 500 hPa reaches its minimum, indicating a moist midtroposphere, around 6 am. It picks up quickly after that and stays at a relatively high value past 12 pm. The vertical velocity w starts negative with a minimum value of −0.4 m/s and then quickly increases passing the zero threshold around 3 am. It remains positive during the rest of the day, reaching its highest values slightly after 6 pm. While the transition from negative to positive at 3 am coincides with a near CIN minimum, the decreasing dryness suggests that convective activity has triggered the upward motion. On the other hand, the persistence of positive w during the evening is an indication of a large-scale upward motion dominated condition. *Inv* remains the variable that seems to vary the most with very little to no correlation with the other indicators; nonetheless, we note a rapid increase and strongest peaks right after 6 am.

Accordingly, the corresponding area fractions shown on the left columns of Figure 4 indicate a congestus-dominated condition prior to 6 am with a peak at roughly 3 am. Deep convective area peaks slightly before 6 am, while stratiform rain area shows a gradual increase through the morning hours to peak at about 8 am and somewhat plateaus thereafter to suddenly plunge down around 3 pm. We note that while the burst in deep convection before 6 am coincides roughly with the first CAPE maximum and first CIN minimum, the secondary extrema in those variables at 6 pm are not accompanied by convection of any sort as the area fractions remain low—near zero—after 6 pm. The cloud area fractions are more consistent with dryness, which shows consistently high values during this period and a single minimum around 6am. This is a demonstration why CAPE alone cannot be used as an indicator of deep convection. Moreover, the fact that the vertical velocity remains positive during the rest of the day once it crosses zero around 3 am warrants against the use of this parameter as a positive indicator of deep convection as done in Peters et al. (2013). Arguably, it is the convection that led to the first peak in w right after 6 pm and not the opposite, while the positive w in the afternoon and evening has nothing to do with local convection as already anticipated. Here we use only the negative part of w as an indicator for suppressed conditions of deep convective and congestus clouds. We note also that the sudden decrease in deep convection after 6 am coincides with the first peak of *Inv* as noted above.

3.4.2. 2 and 3 October: Suppressed Convection

The second testing period from 2–3 October 2011 is characterized by two distinct regimes, as seen in the patterns of CAPE, LCAPE, and CIN (Figure 5). During the first period, there is high CAPE, high LCAPE, and low CIN, and during the second period, there is low CAPE, low LCAPE, and relatively high CIN. During the first day, CAPE and LCAPE peak around 6 am and plateau before they drop sharply at 6 pm to hit their lowest values at the beginning of the second day. They then both increase again at 12 pm the second day, with CAPE presenting a sharp secondary peak at roughly 9 am. CIN has its lowest minimum around 12 pm during the first day and its highest peak at the beginning of the second day. Dryness also shows a similar

Table 2
Transition Time Scales Used or Obtained in Previous Studies for the Same Cloud Transtions: Khouider et al. (2010; KBM10, 2 cases), Frenkel et al. (2012; FMK12), Peters et al. (2013; P2013) and De La Chevrotière et al. (2016; D2015: 2 × 2 and 4 × 4 partitions)

Study	KBM10			P2013			D2015	
Time scales	Case 1	Case 2	FMK12	C_c	C_{Cr}	C_ω	2 × 2	4 × 4
τ_{12}	1	2	1	3	1.2	1.2	0.208	0.238
τ_{23}	3	0.5	3	0.13	0.16	0.16	0.359	0.2570
τ_{10}	5	2	1	1	1.2	1.2	7.426	1.761
τ_{20}	5	5	3	5	2.2	2.4	10.126	9.551
τ_{30}	5	24	5	5	4	4	1.444	1.021
τ_{01}	1	3	1	1	1	1	27.686	31.789
τ_{02}	2	5	3	4	2.2	2.2	17.950	11.821

Note. For P2013, the C_c, C_{cr}, and C_w correspond to whether CAPE, low-level CAPE, or vertical velocity was used as indicator for deep convection, respectively.

pattern, with low values (a moist atmosphere) during the first day reaching below 0.4 at 6 pm and high values (a dry atmosphere) during the second day with a plateau near 0.7 after hour 30 or 6 am the second day.

Vertical velocity shows a similar pattern with lowest values during the first day and highest on the second (Figure 5). We particularly note the two minima in *w*, characterized by velocities of about −0.1 m/s around 6 am and 9 pm the first day. The *Inv* predictor also shows a consistent pattern, although there are some fluctuations. We have mostly high *Inv* values during the first day, between 6 am and 6 pm, and low *Inv* values between 9 pm the first day and 12 pm the second day. We note that while the high CAPE, low CIN, and low dryness are meant to favor convection on the first day, the low CAPE, high CIN, and high dryness will likely inhibit convection. The occurrence of negative *w* values together with high *Inv* values has the tendency to disfavor convection during the first period also.

Consistently, the area fraction plots show very low and very sporadic deep convection not exceeding 0.01 (Figure 5). Congestus and stratiform areas seem to be more present overall with similarly many various peaks but they are also low, around 0.04 for congestus and between 0.1 and 0.2 for stratiform. These are much lower values compared to the maxima seen on 16 October. Convection seems to be inhibited during the first day because of high *Inv* and negative vertical velocities, while its weakness during the second day is likely due to high dryness, low CAPE, and high CIN values.

3.4.3. 19–22 October: Active MJO

The large-scale predictors corresponding to 19–22 October 2011 are shown ion the right column of Figure 6. They are grossly characterized by three separate periods in terms of CAPE and dryness. There are two periods favorable for deep convection, one between midnight of 19 October and 6 am of 20 October and another beginning midnight of 21 October. They are separated by a period of low CAPE, low LCAPE, high CIN (exceeding 15 J/kg), and particularly high dryness that peaks at 12 pm on 20 October with a maximum of near unity (*RH* down to nearly 50%). This inhibition period is also characterized by high fluctuations in vertical velocity, which twice reach below zero values of nearly −1 m/s. The two favorable periods for convection at the beginning and the end of the time series depict coherently positive *w*. Similar to the 16 October case, *Inv* seems to display an uncorrelated pattern with a few ups and downs that seem to be random. Consistently, the data records for this period, reported on the left panels of Figure 6, show three peaks in congestus and deep convection area fractions, suggesting a persistent diurnal cycle consistent with the work of Ruppert and Johnson (2015) who found that diurnal variability of cumulus convection helps the moistening of the atmosphere during the MJO onset stage. However, consistent with our observation made above, the deep convection peak is much weaker during the dry/unfavorable period between 6 am on 20 October and midnight on 21 October, while the three congestus peaks have comparable magnitudes. As for the single peak on 16 October, the congestus peaks always lead deep convection by a few (3–5) hours. As expected, three stratiform area fraction peaks follow the deep convection peaks by 3 to 6 hr. We note also that consistent with the deep convection time series, the stratiform middle peak is weaker.

The three time periods provide different testing conditions, not only in terms on the lengths of the observed time series, which are crucial for the Bayesian inference procedure as shown in De La Chevrotière et al.

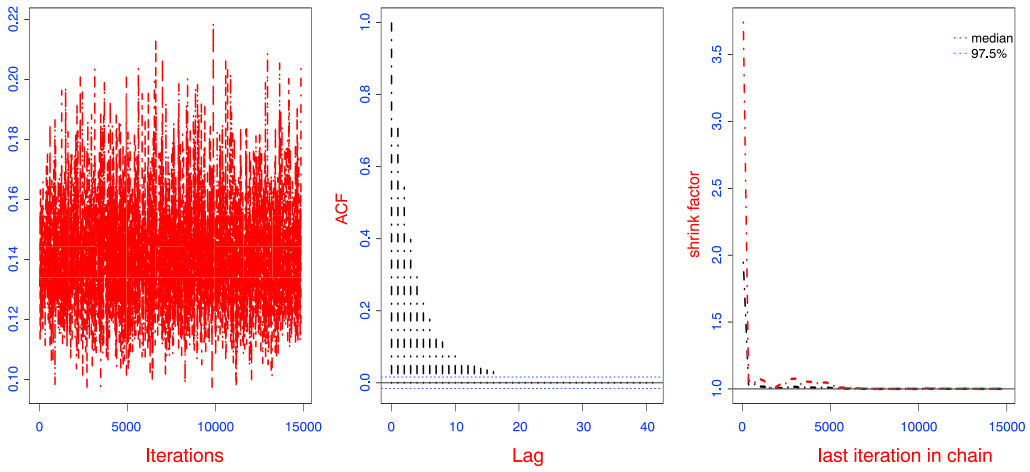

Figure 7. Convergence diagnostics ($T = 144$) for the Markov chain τ_{23}, (left) traceplot ($T = 144$), (middle) autocorrelation, and (right) Gelman plot showing the evolution of the shrink factor as the number of iterations increase.

(2014), but also in terms of large-scale conditions that exhibit various scenarios including both active and inactive periods of the MJO. Both the behavior of the cloud area time series in Figures 4–6 and their complex relationships seem to be consistent with the two main hypotheses of the extended SMCM described in the previous section, namely, that the clouds transition randomly from one state to another and the probabilities of transition are preset by the environmental conditions that can be represented by the five selected indicators. Moreover, the likelihood of the high probability of transition from congestus to deep convective and then from deep convective to stratiform clouds with a seemingly universal time scale is evident. It is the task of the Bayesian inference to determine these time scales for the provided data and thus quantify the associated transition probabilities and their assumed dependence on the selected large-scale indicators.

4. Results

4.1. Estimation of Model Parameters Using the Bayesian Inference Method

In this section we present the results of the Bayesian inference method when applied to infer the transition time scales for the SMCM from the DYNAMO SMART-R and sounding data described above. The obtained time scales are compared to those used or obtained in previous studies and the ability of the SMCM to reproduce the observed cloud fractions using the inferred parameters is assessed.

Based on observations and model simulations of tropical convection, the lifetime of a typical tropical cloud is estimated to be on the order of a few minutes to a few hours (Johnson et al., 1999; Waite & Khouider, 2010). In general, the formation of a cloud is much faster than that of its decay (Khouider et al., 2010). Also, the decay of stratiform clouds is believed to be much slower than that of either a congestus or a deep cloud. In Table 2, we recall various sets of SMCM transition time scales that were reported in previous studies. Some of them are somewhat arbitrary and based purely on physical intuition, while others were based on data and/or simulation results.

The values in Table 2 for the time scales reported in the first two columns from the left (KBM10, cases 1 and 2) are those used in the original SMCM paper (Khouider et al., 2010). They are reviewed here for purely historical reasons. They are prescribed based on physical intuition and general qualitative knowledge about the formation and decay of clouds in the tropical atmosphere. In Frenkel et al. (2012), the KBM10 time scale parameters were adjusted slightly to allow a good performance when simulating moist gravity waves. The latter are reported on the third column (FKM12). They are further modulated by a proportionality adjustment parameter t_{grid} to allow a systematic dependence on the GCM resolution. The values of the fourth to sixth columns are those obtained by Peters et al. (2013) for the case of monsoon convection over Darwin, Australia. They are derived by visually fitting the SMCM's equilibrium cloud area fraction distribution with the observed convective activity. Peters et al. (2013) tested and compared various combinations of large-scale predictors. Those reported in Table 2 use $C_c = CAPE$, $C_{Cr} = 2LCAPE/CAPE$, and $C_\omega = (1/10)\,\text{hPa}^{-1}\omega_{500}$, where the pressure-velocity at 500 hPa is used as an indicator for large-scale upward

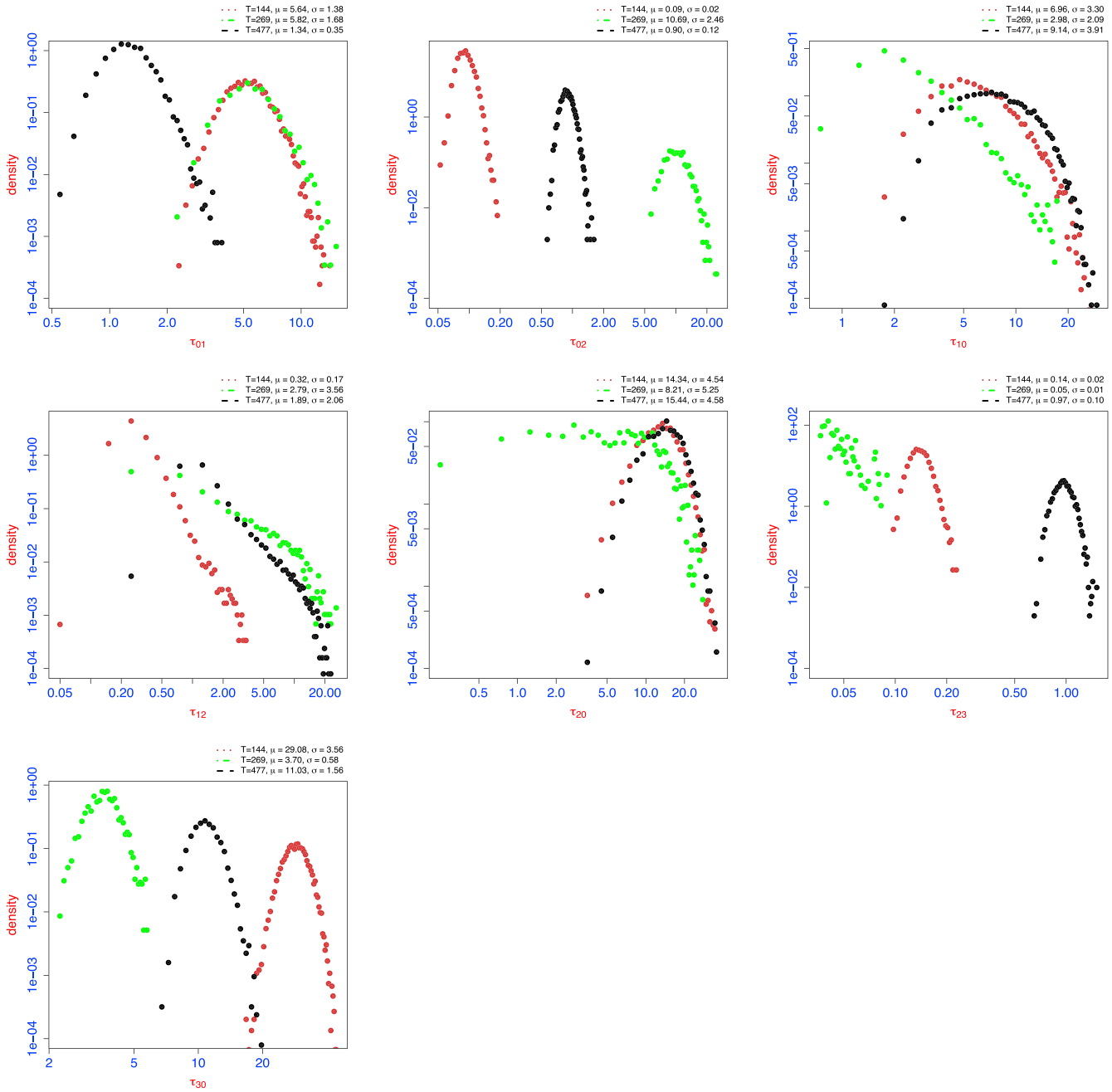

Figure 8. Marginal posterior densities for the time scale parameters τ_{kl} (hr; log-log scale) for the three samples of data $T = 144$, $T = 269$, and $T = 477$, corresponding respectively to the, 16, 2–3, and 19–22 October test cases. The means (μ) and standard deviations (σ) reported in Table 3 are redisplayed here on the corresponding panels.

motion which is assumed to trigger convection. Peters et al. (2013) found the latter to be a better indicator of deep convection when compared to either CAPE or low-level CAPE. This result may be due to the presence of large-scale forced monsoon convection, which may differ from the case of the MJO onset or preonset considered in the current study.

De La Chevrotière et al. (2016) used the Bayesian method, discussed above with only *CAPE*, *LCAPE*, and dryness predictors, to infer the SMCM transition time scales from a 24-hr LES (Giga-LES Khairoutdinov et al., 2009). To expand the length of the Giga-LES time series, De La Chevrotière et al. divided the 200×200

Table 3
Summary Statistics Obtained for Each of the Transition Time Scales When the Bayesian Approach Is Applied to Three Different Samples of Data: 16 October (MJO, initiation $T = 144$), 2–3 October (suppressed convection, $T = 269$), and 19–22 October (active MJO, $T = 477$), See Text for Details

Time scales	Mean	SD	Naive SE	Time series SE
		$T = 144$ (1 day)		
τ_{12}	0.32	0.19	1.081e-03	0.0056922
τ_{23}	0.14	0.02	9.555e-05	0.0002522
τ_{10}	6.96	3.30	1.914e-02	0.0650757
τ_{20}	14.34	4.54	2.635e-02	0.0699022
τ_{30}	29.08	3.56	2.067e-02	0.0500940
τ_{01}	5.64	1.38	8.022e-03	0.0224946
τ_{02}	0.09	0.02	8.801e-05	0.0003088
		$T = 269$ (~2 days)		
τ_{12}	2.79	3.56	0.0466749	0.182932
τ_{23}	0.05	0.01	0.0001339	0.001449
τ_{10}	2.98	2.09	0.0273470	0.108296
τ_{20}	8.21	5.25	0.0687849	0.177657
τ_{30}	3.70	0.58	0.0075476	0.020089
τ_{01}	5.82	1.68	0.0219738	0.054028
τ_{02}	10.69	2.46	0.0322189	0.093343
		$T = 477$ (3.25 days)		
τ_{12}	1.89	2.06	0.0130038	0.060308
τ_{23}	0.97	0.10	0.0006582	0.002232
τ_{10}	9.14	3.91	0.0246425	0.099420
τ_{20}	15.44	4.58	0.0288696	0.068749
τ_{30}	11.03	1.56	0.0098305	0.030181
τ_{01}	1.34	0.35	0.0022289	0.006860
τ_{02}	0.90	0.12	0.0007355	0.002964

Note. (from left to right) Mean, standard deviation (SD), naive standard error (SE) of the mean, and time series standard error (SE) of the posterior marginal distributions.

km^2 LES domain into either 2×2 or 4×4 partitions. The resulting time scales are reported in the last two columns of Table 2 (2×2 and 4×4 partitions).

The Bayesian inference approach described above is applied to the three samples of data of sizes $T = 144$, $T = 269$, and $T = 477$ reported above where the MCMC chains were monitored for convergence on the fly (De La Chevrotière et al., 2014). In particular, we performed quantitative and qualitative convergence analysis using the R package MCMCpack to ensure an acceptance rate around 25% and analyzed the trace plots autocorrelations using diverse tests: Geweke, Gelman Rubin, and Heidelberger and Welch (1981) to the obtained posterior distributions $p(\mathbf{\Phi}|y_i)$. The corresponding trace, autocorrelation, and shrink factor plots are shown in Figure 7 for the $T = 144$ test case, for the sake of illustration. When the tests indicated no evidence against the null hypotheses, we drew samples from the corresponding posterior distributions and computed their summary statistics.

In Figure 8, we plot the marginal posterior densities for the time scale parameters for the three data samples $T = 144$, $T = 269$, and $T = 477$. For the transition time scales τ_{12}, τ_{10}, τ_{20}, and τ_{12}, the posterior densities of these three different samples of data show some degree of similarity between two or all test cases, but there also many discrepancies, especially for the rest of the time scale parameters. Each one of the three test cases has its own mean cloud area fraction and distribution leading to different transition time scales. As seen in Peters et al. (2013), the transition time scales depend strongly on the background climatology consistent

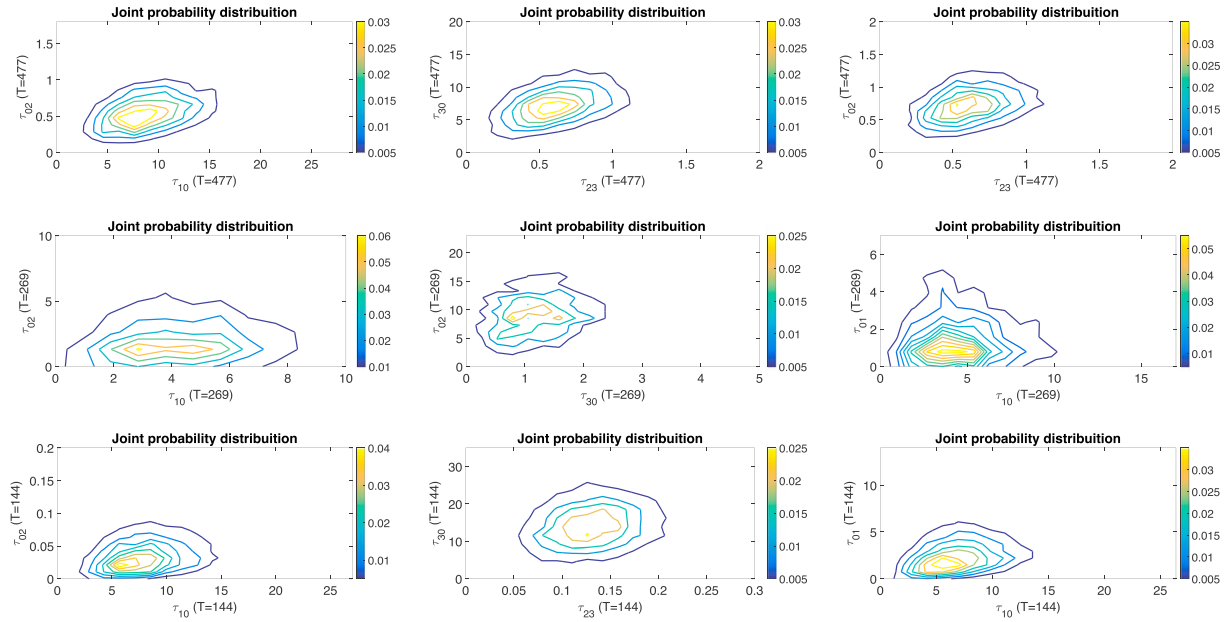

Figure 9. As in Figure 8 but for joint marginal distributions for three distinct pairs of timescale parameters for the three training periods.

with the fact that the model's equilibrium distribution depends exclusively on the transition rates (Khouider et al., 2010).

According to theory, large enough data samples would lead to convergence to a stationary distribution independent of the prior distribution. From this perspective it might be reasonable to run the Bayesian approach with a larger data set, such as the entire 4-month SMART-R data set, to obtain a somewhat universal set of transition time scales for the MJO, if adequate computing resources were made available.

The associated means, standard deviations, and statistical errors of the estimated time scales are reported in Table 3 for the three chosen test cases. A comparison can now be made with the results obtained in previous studies reported in Table 2. The means of the marginal posterior distributions of τ_{12} in Table 3 are within the range of those reported previously as shown in Table 2. The mean τ_{23} value is comparable to the values in Peters et al. (2013), De La Chevrotière et al. (2016), and KBM10-Case 2 in Khouider et al. (2010). For τ_{10} only, case 1 in KBM10 and the 2×2 partition of De La Chevrotière et al. (2016) present similar values to those obtained in this study. The mean value τ_{20} obtained here is higher than the highest value reported in De La Chevrotière et al. (2016). Since the majority of the means indicate that at least 5 hr are necessary for this transition, it is expected for this transition to be slow. The mean values for τ_{30} are different from each other and from the previous studies; some of the results indicate 2, 4–5, and even 24 hr compared with 3.69, 11.03, and 29.08 found in Table 3. The mean value for τ_{01} obtained using $T = 477$ is comparable to case 1 of KBM10, FMK12, C_c, C_{rC}, and C_ω of Peters et al. (2013). All the other values are very different. From the mean values for τ_{02}, it might be difficult to draw conclusions as the values are very far apart. However, τ_{30} for $T = 477$ is close to the value of 11.8 hr obtained in the 4×4 partition of De La Chevrotière et al. (2016).

We note in particular that, for the transition from congestus to deep (τ_{12}), most of the inferred values are found between 1 and 2 hr. The decay time of congestus (τ_{10}) has values between 5 and 7 hr although the posterior density for $T = 477$ shows a larger variance compared to the one for $T = 144$. For the decay of deep, τ_{20}, the density functions estimate a time of 15 hr approximately, while congestus birth time scale is between 4 and 6 hr. For the rest of the transition time scales, it is rather difficult to make assumptions about a "universal time scale" for the different transitions between different clouds and clear sky. For this purpose, it will be necessary to run the model for a longer period of time.

A question of interest is to see whether the inferred time scales are correlated with each other. In Figure 9, we plot the joint marginal distribution between three distinct pairs of time scales for the three training periods, namely, (τ_{02}, τ_{10}), (τ_{30}, τ_{23}), and (τ_{02}, τ_{23}). Interestingly, while all three pairs show some degree of (linear) correlation, as suggested by the obliqueness of the associated contours, during both the initiation

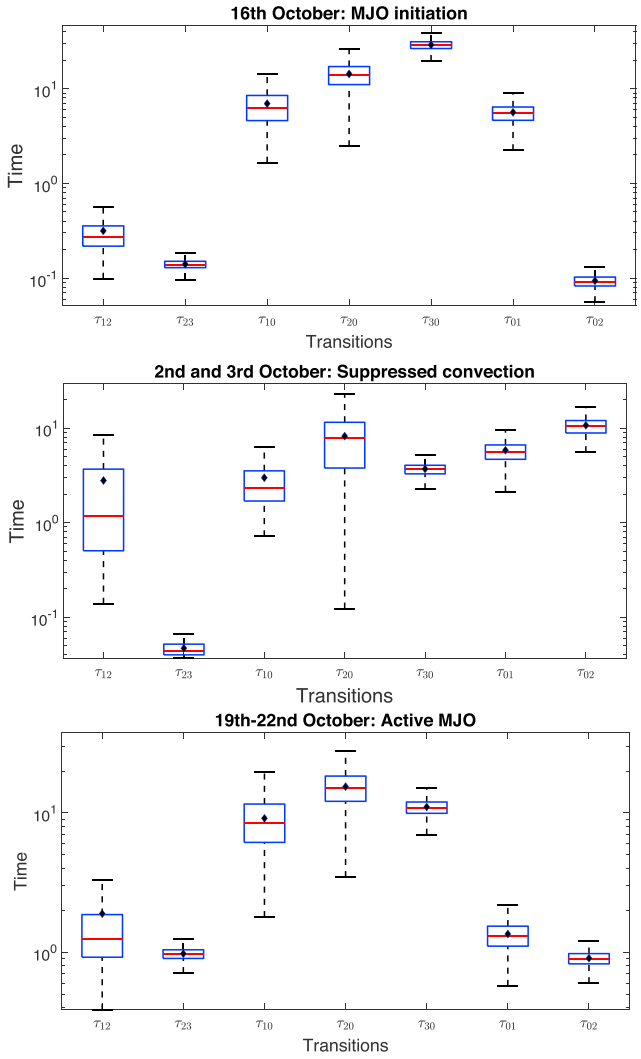

Figure 10. Boxplots of the marginal posterior (time in hr, in log scale). See text for details. (top) $T = 144$, (middle) $T = 269$, and (bottom) $T = 477$. MJO = Madden-Julian Oscillation.

($T = 144$, bottom panels) and active ($T = 477$, top panels) phases, those inferred during the suppressed phase ($T = 269$, middle panels) seem to be totally uncorrelated with one another. While the linear correlation during the active period may be helpful when tuning the SMCM for a GCM, the fact that the parameters are uncorrelated during the suppressed phase may be a symptom of the chaotic and unorganized character of convection during this MJO phase, that is, the cloud states do not happen concurrently. Moreover, the lack of correlation may be viewed as a good thing in terms of parameter sensitivity as this might indicate that those parameters can be tuned independently.

A comprehensive visual perspective of the marginal distribution of the inferred time scales is given by the boxplots in Figure 10 for the three test cases. For clarity, the plots are separated into groups of fast (≈1 hr or less) and slow (many hours) time scales. The horizontal red lines represent the median values, the black dots represent the mean values, and the blue boxes delimit the 50% interquartile range. The dark vertical lines represent the 75% interquartile range.

Hohenegger and Stevens (2013) used satellite observations over the tropical region between 30° S and 30° N and between 70° W and 30° E in May 2010 and found that the transition from shallow to deep convection takes about 4 hr over ocean and 2 hr over land. Another study (Kumar et al., 2013) over Darwin suggests that congestus clouds appear about 10 hr before the peak of the rainfall maximum and (some of them) are still present 2 hr after the rainfall event. It is also stated that the maximum for deep cloud populations occurs shortly after the rainfall peak. Although these studies did not specifically provide birth and death time scales in the sense of the SMCM, the aforementioned times can be used as bulk measures for the respective cloud lifetimes and can thus be used as rough upper bounds for our Bayesian estimations. Considering the upper quartile of each of the boxplots in Figure 10 for the three different samples of data, 75% of the inferred values fall below 24 min for 16 October ($T = 144$), 75% fall below 4 hr for 2–3 October ($T = 269$), and 75% of the inferred values fall below 2 hr for 19–22 October ($T = 477$).

In the present study, while 75% of the inferred time scales fall roughly under 40 min and are classified as "fast transitions" (Figure 10), they show considerable variations from case to case. For the transition from deep to stratiform parameter, τ_{23}, for example, the 75% interquartile shows inferred values of under 10 min for the 16 October case, under 3 min for the 2–3 October case, and just under 1 hr for the 19–22 October case, while in De La Chevrotière et al. (2016), the corresponding values are below 20 min (see Table 2). The time that a congestus cloud takes to decay, that is, τ_{10}, has an upper quartile of under 9 hr for the 16 October case, 4 hr for the 2–3 October case, and 12 hr for the 19–22 October case (Figure 10). In De La Chevrotière et al. (2016), the time estimated is under 10 hr, which is consistent with our results. Our analysis indicates that the time scale obtained for the decay of deep clouds τ_{20} can take up to 18 hours: 18 hr for 16 Octover, 17 hr for 2–3 October, and 12 hr for 19–22 October. These results agree with the results obtained in De La Chevrotière et al. (2016) who characterized this transition as "slow."

Concerning the decay of stratiform τ_{30}, the differences are large (Figure 10). While in the previous Bayesian inference study, it can take up to 1.5 hr; our results show longer times for this cloud process: 33 hr for 16 October, 4 hr for 2–3 October, and 12 hr 19–22 October. This is consistent with the studies of Deng et al. (2016) and Ajayamohan et al. (2016) who ran sensitivity experiments regarding the ability of the SMCM, when used as a convective parameterization in an idealized aquaplanet GCM, to simulate organized convection on various scales. They found that a longer τ_{30} value leads to good MJO and monsoon intraseasonal oscillation simulations, while a shorter τ_{30} yields synoptic scale convectively coupled Kelvin waves and westward moving monsoon low pressure systems. In terms of the data sets used by the Bayesian inference method,

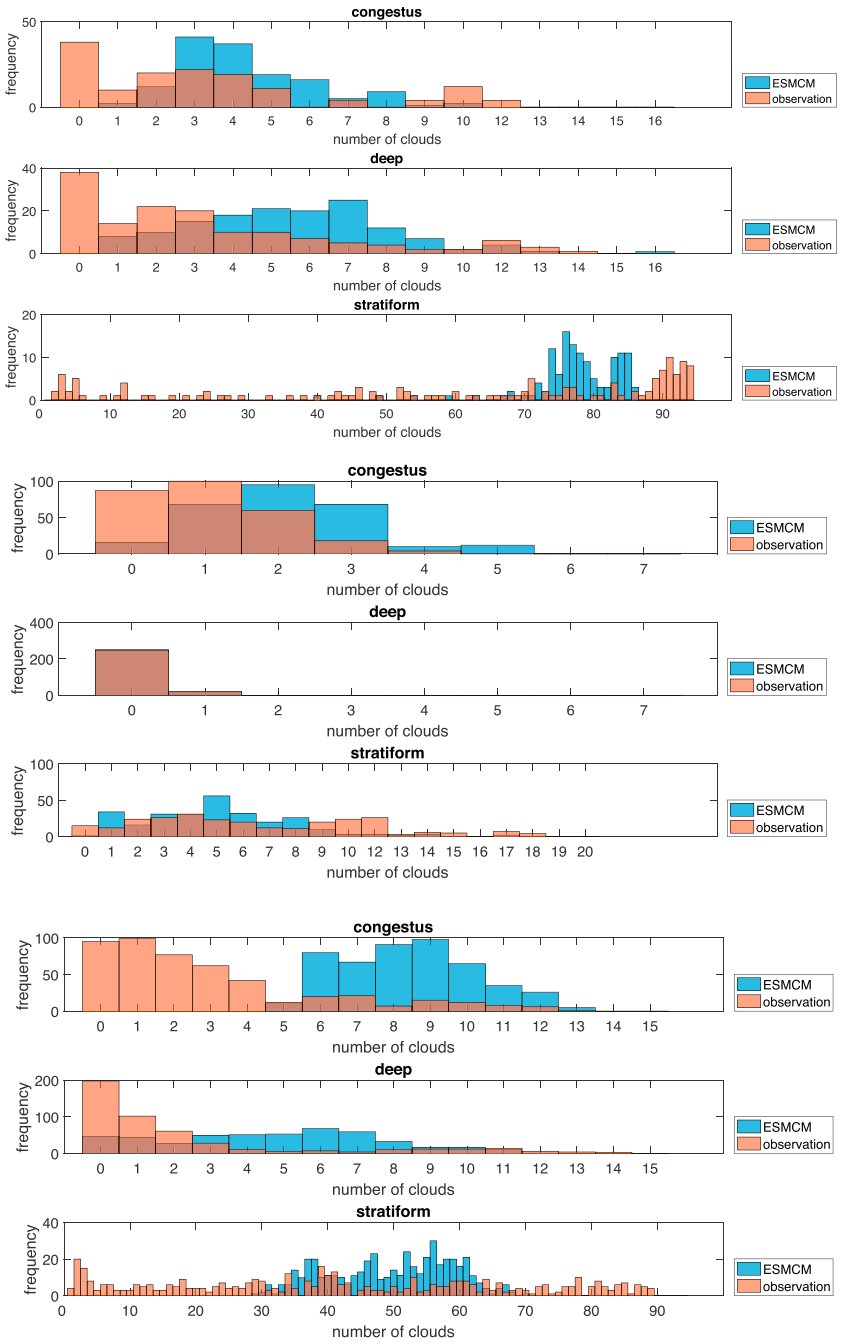

Figure 11. Frequency histogram displaying the number of cloudy pixels denoted by "number of clouds" of the observational (orange) and simulated (blue) cloud number for the clouds congestus, deep and stratiform for $T = 144$ (top), $T = 269$ (middle), and $T = 477$ (bottom). The overlapped rectangles appear in brown color.

this discrepancy can be related to the fact that the Giga-LES simulation was performed for a convection case over the topical Atlantic during the GATE field experiment, which is known to be characterized by African Easterly waves, while the DYNAMO data coincide with an MJO event.

Regarding the formation of congestus time scale, τ_{01}, again in terms of the upper quartile in Figure 10, the estimated values can reach up to 7 hr for the 16 and 2–3 October cases and down to 1.5 hr for 19–22 October. This variability is consistent with the fact that the MJO suppressed phase is more favorable to congestus clouds. It is also worthwhile mentioning that in Deng et al. (2016), a good simulation of the MJO by the SMCM-aquaplanet GCM was contingent on the use of a large value (on the order of a few days) for the

Table 4
Mean Cloud Area Fractions of the Observations and Stochastic Multicloud Model Simulation for the Three Test Cases (See Text for Details)

	$T = 477$		$T = 269$		$T = 144$	
	$n^2\bar{\sigma}_{\text{obs}}$	$n^2\bar{\sigma}_{\text{model}}$	$n^2\bar{\sigma}_{\text{obs}}$	$n^2\bar{\sigma}_{\text{model}}$	$n^2\bar{\sigma}_{\text{obs}}$	$n^2\bar{\sigma}_{\text{model}}$
Congestus	2.97	8.42	1.07	2.08	3.29	4.33
Deep	2.25	4.72	0.07	0.06	3.31	5.54
Stratiform	42.10	49.62	6.60	5.03	62.08	78.03

formation of congestus. However, it is important to note that in Deng et al. (2016), the extradependence of the associated transition rate on CIN, Inv, and vertical velocity were lacking.

The last transition to be discussed is that of the formation of deep clouds, τ_{02}. The resulting values for this transition time scale vary considerably in Figure 10. For the 16 October case, the formation of deep clouds takes place within minutes (upper quartile lies near 10 min), but for 2–3 October case, it can take up to 12 hours, while for 19–22 October case, this transition takes around 1 hr. These numbers are consistent with the different MJO phases that these test cases represent. In De La Chevrotière et al. (2016), this transition is a "slower transition" where the upper quartiles lie between 12 and 30 hr (Table 2).

4.2. Stand-alone SMCM Simulation Tests

We now make a direct comparison of the SMCM predictions against the SMART-R observations of precipitating cloud type. In a way, this is how we assess whether the Bayesian inference has worked or not. This is a more decisive test than simply comparing the newly calculated time scales to those from previous studies as done in the previous subsections. The simulations presented here are done in a stand-alone mode where the stochastic cloud model is forced by the observed large-scale predictors corresponding to the three training periods while the feedback to large-scale environmental state is ignored. Thus, the numerical tests presented are far from being definitive since in an actual GCM such feedback will certainly play an important role in the course of the cloud simulation. However, these idealized tests will provide a rough idea on whether the SCMC can provide realistic cloud area fraction dynamics in this idealized situation.

More precisely, we run the stand-alone extended SMCM using each of the inferred transition time scale sets and the associated DYNAMO predictor values corresponding to each of the three test cases above. Ideally, we would train the model on a large enough data set to obtain a universal set of transition time scales and then test them on different data sets. However, since the present time scales are far from being universal, we limit ourselves to a minimalistic testing asking simply whether the SMCM is capable to reproduce the cloud time series that it was trained on.

The right panels of Figures 4–6 show the three cloud type area fraction time series simulated by the stand-alone SMCM for the 16 October (MJO initiation), 2–3 October (suppressed convection), and 19–22 October (active MJO) test cases, respectively. Compared to the observed time series on the left panels, we can see that the SMCM simulations reproduce some qualitative and quantitative features of the SMART-R area fractions. For instance, the consecutive congestus and deep convection peaks early on 16 October (MJO initiation) in Figure 4 are captured. The transition to large stratiform areal coverage is also well captured. However, unlike the observations, there is no rapid decrease after 15 hr in the SMCM simulation. This is likely due to a combination of the slow stratiform time scale of 29 hr reported in Table 3 and the fact that the model simulation has a secondary peak in deep convective clouds between 15 and 20 hr, which is responsible for maintaining a source of stratiform cloud. It is also worth mentioning that the lack of large scale dynamical feedback in another drawback of this study.

Similarly, for the 19–22 October (active MJO) case in Figure 6, we see coherent fluctuations characterized by a succession of peaks in congestus cloud occurrence followed by deep convective and then stratiform area peaks. However, unlike the observations, the model's congestus and stratifrom area fractions do not decrease appreciably in between peaks. Also, the simulated deep convection events have longer lifetimes. The secondary convection peak corresponding to the dry conditions of the second day (between 24 and 48 hr) is somewhat reproduced in the model results by displaying a weaker peak at 36 hr but not as weak as in the observations.

The 2–3 October case (suppressed convection; Figure 5) is perhaps the most well represented by the model in the sense that, just like the observations, the model produces only a few sporadic peaks in deep convection and somewhat more coherent and extended congestus and stratiform events, though the phase is off, suggesting more of a chaotic nature. This is consistent with the findings of Peters et al. (2013) who demonstrated that, in both the observations and the SMCM, convection tends to be more chaotic when the mean rainfall is small and more organized when the mean rainfall is large.

Based on Figures 5–8, the SMCM appears to do a reasonable job in reproducing the different maximum ranges in each cloud type area fraction corresponding to the three different tests. To further quantify the areal coverage comparison, we report in Table 4 the mean area fraction values associated with each test case for both the observations and the model results. The simulated mean area fractions compare reasonably well with their observed counterparts, except perhaps for the deep and congestus cloud types in the $T = 477$ case for which the simulated mean area fractions are double the observed, consistent with the more persistent and elongated convective events produced by the model.

To further test the performance of the SMCM, we compare the frequencies of events (number of clouds) for each of the cloud types by plotting in Figure 11 the frequency histograms of the model simulations and the SMART-R observations. The model seems to be able to simulate comparable numbers of event types for most cases compared to observations, except for the $T = 477$ test case, which shows a systematic overestimation of large events. This result is consistent with the aforementioned extended lifetimes of the convective events. The model has a hard time predicting zero number of clouds for many of the cases/cloud types, this is maybe related to a low sensitivity to the predictors. This can be alleviated by tuning the normalization constants of these predictors and will be the subject for future research as pointed out in section 5.

5. Conclusion

A Bayesian procedure was applied to sounding and radar observations made during the DYNAMO field campaign in order to infer key parameters for the SMCM of Khouider et al. (2010). The field campaign took place in the central Indian Ocean in order to understand the key dynamical processes responsible for the initiation and propagation of the MJO (Yoneyama et al., 2013). Between October 2011 and January 2012, the DYNAMO experiment witnessed the occurrence of three MJO events: one in October, one in November, and one in late December/early January. The SMCM uses a set of large-scale predictors to emulate the probabilistic evolution of the area fractions of three key cloud types, namely, congestus, deep convective, and stratiform, in the form of a stochastic birth-death process whose transition probabilities are conditional on the large-scale predictors. The SMCM uses a large number of unknown parameters including a set of so-called transition time scales that are used to modulate the transition probabilities of the stochastic process. Despite these uncertainties, the SMCM has been successfully used as a parameterization of organized convection in both simple models and state-of-the-art global climate models (Ajayamohan et al., 2016; Deng et al., 2015; Frenkel et al., 2012; Goswami et al., 2017b).

The Bayesian technique, developed and assessed against synthetic and LES data by De La Chevrotière et al. (2014, 2016), aims at learning the SMCM transition time scales using cloud area fraction time series in order to improve quantitatively the performance of the SMCM parameterization and reduce the number of tuning parameters. Cloud area fractions from the SMART-R C-band mobile radar deployed during DYNAMO were combined with observations from the DYNAMO sounding array located in the vicinity of the Maldives archipelago where the C-band radar was operating. The sounding data were used to obtain the large-scale predictors that were used to drive the SMCM and the Bayesian inference operation. Due to the computation burden, only three small subsets of length 1 to 3 days were used. They correspond to the suppressed (2–3 October), initiation (16 October), and active (19–22 October) phases of the October MJO. Transition time scales corresponding to each testing period were inferred and compared with each other and with those used or obtained in previous studies (De La Chevrotière et al., 2016; Frenkel et al., 2012; Khouider et al., 2010; Peters et al., 2013). In addition, the SMCM was run for each test case in a stand-alone mode using the inferred transition time scales and forced with the corresponding DYNAMO predictors, and the resulting cloud area fraction time series were compared to the SMART-R radar data.

Despite the crudeness of these preliminary tests based on small data samples, a good deal has been learned about the performance of the Bayesian methodology and the SMCM itself. First, the inferred time scales

were in the bulk range of a few minutes to a few hours, which is generally consistent with previous studies although some of the time scales vary greatly from one test case to another. As shown in Table 3, the transition time scale from congestus to deep convection, τ_{12}, varies from 0.3 hr during the initiation phase to almost 2 hr during the active phase to nearly 3 hr during the suppressed phase. While there is a tendency of convergence as we move from the small 1-day sample to the larger multiday samples, the fact that the suppressed phase yields a larger τ_{12} is consistent with the fact that convection (including congestus) is in general weak during this period, which is characterized by unfavorable large-scale conditions as pointed out in section 3.4. This point is more evident when comparing the time scale of the direct formation of deep convection from clear sky, τ_{02}, which varies from about 5 min for the initiation phase to almost an hour for the active phase to more than 10 hr for the suppressed phase. The decay of deep convection time, τ_{20}, on the other hand seems to vary less. It is about 14 and 15 hr during the initiation and active phases and about 8 hr during suppressed conditions. While the smaller latter values are consistent with the physics, the associated variabilities, as shown by standard deviations, the marginal distribution in Figure 8, and the boxplots (Figure 10) display a great deal of overlap.

Whereas there are both qualitative and quantitative similarities between the transition time scale corresponding to the different test cases and previous studies, the Bayesian method is highly dependent on the training data set and the underlying convection regime. For example, the birth rates of deep versus congestus clouds tend to be higher than one another depending on whether we are in the presence of a convectively active or suppressed weather state. Ideally, the Bayesian method would yield a universal set of transition time scales that are valid over all possible weather states, while the inherent variations in the transition rates should be captured by their assumed dependence on the large-scale predictors through the Γ function combinations. Viewed purely from this angle, the present study may seem obsolete since the inferred values span quite large ranges of values. However, this high variation indicates how much sensitivity we need to put into the Γ function in order to capture these regime changes by the sole dependence on the large-scale indicators so that the effective transition time scale, given by

$$\tau_{kl}^{\text{eff}} := \frac{1}{R_{kl}} = \frac{\tau_{kl}}{\Gamma_{k,l}(Ind1, Ind2, \ \dots\ )},$$

where $\Gamma_{k,l}(Ind1, Ind2, \ \dots\ )$ is a generic notation to indicate the dependence of the transition rate on the set of large-scale predictors. For instance, we need the associated functional $\Gamma_{k,l}(Ind1, Ind2, \ \dots\ )$ to decrease by up to two orders of magnitude to allow a change of the effective time scale for the birth of deep convection from a few minutes for the active phase of the MJO and a few hours for the suppressed phase. More importantly, universal time scales are guaranteed only if the training period spans both convectively suppressed and convectively active phases. The present results will be used to motivate a more comprehensive experiment using the full DYNAMO data set, and the results will be reported elsewhere.

In the same vein, the inferred parameters would in principle yield the right statistics of the cloud area fractions given the large-scale predictors. However, it may happen that the climate model may not operate with exactly the same "range" of values in the high-dimensional manifold on the large-scale predictors, as the observations. However, unlike purely data-driven technics that rely heavily and only on data (Brenowitz & Bretherton, 2018; Dorrestijn et al., 2013; Gentine et al., 2018; Schneider et al., 2017), the functional form of the transition probabilities in equation (7) allows a smooth extrapolation of these probabilities outside the observational range. In this regard, the Bayesian procedure as utilized here can be regarded as an interpolation-extrapolation problem of the transition rates with basis functions based on the expression in equation (7). This is indeed confirmed with the success of the recent implementation of the SMCM in the Climate Forecasting System v2 by Goswami et al. (2017c) based on the time scale parameters obtained in De La Chevrotière et al. (2016).

We have also conducted, in section 4.2, idealized numerical tests where the extended SMCM was run in a stand-alone mode by simply forcing the cloud model by the observed predictors ignoring the feedback to the large-scale variables. These idealized stand-alone SMCM runs demonstrate that the SMCM is capable of reproducing some important features of the observed cloud fraction time evolution during the various regimes of MJO convection. The range of variability of the different area fractions is well captured, such as the large deep convection peaks of nearly 15% during the initiation and active MJO periods that decrease to 1% during the suppressed phase. The sporadic deep convective activity during this last period is also well simulated. The same can be said about the congestus and stratiform area fractions. However, the phasing

and the number of peaks show important discrepancies when compared to the observations. The deep convection, for instance, has a secondary peak in the evening of 16 October that is not observed in the SMART-R data, and consequently, the model is unable to capture the observed evening depletion of stratiform. This is maybe due to the model's over reliance on CAPE and being less sensitive to dryness, which is much higher during that period as shown on Figure 4. Similarly, for the active phase testing period, corresponding to 19–22 October (Figure 6), while the model captures some features of the observed cloud area fraction time series, it lacks the observed large variations of area fraction with the convective activity, which does not come all the way down to zero as in the observations. Although weak, the model does show a decrease in both deep and stratiform fractions between 30 and 54 hr consistent with the SMART-R data. The overall good performance of the SMCM stand-alone runs during the different regimes is consistent with the results obtained when the SMCM was used as parameterization in a GCM subject to a proper tuning of the time scales (Ajayamohan et al., 2016; Deng et al., 2016).

While the preliminary results obtained by the first application of this Bayesian approach to learn the transition time scales for the SMCM are encouraging, the less than optimal performance is perhaps associated with the lack of sensitivity to the large-scale predictors. This issue can be addressed by retuning the rescaling constants CAPE_0, CIN_0, T_z, and W_0 in order to obtain a more realistic sensitivity of the transition rates in Table 1 with respect to the large-scale predictors. A reformulation of the gamma function in equation (7) and/or the rescaling procedure in equations (1)–(6) is/are also foreseeable. Using CAPE as an example, one could use instead

$$x_{CAPE} = \frac{CAPE}{CAPE_0} + c,$$

where c is the intercept that can made negative to allow a wider range of variability for the Γ function. The prescaling constant CAPE_0 and c could be preset according to a large range of observations spanning a few MJO periods for example. Such preprocessing together with the application of the Bayesian procedure over a larger range of cloud data would lead to a universal set of transition time scale parameters that can be used with confidence in the SMCM parameterization.

Both for logistical reasons (data accessibility) and for the sheer importance of tropical clouds and convection, the present work was restricted to the tropics. To obtain a more universal set or more comprehensive sets of time scale parameters, the model needs to be trained on data sets emanating from other parts of world that are known to have equally large amounts of convective clouds and rain such West Africa, South America, India, and Australia as well as the midlatitude storm tracks. Moreover, the Markovian framework can be extended to include other cloud types such as shallow cumulus and stratoscumulus clouds. This can be easily achieved by extending the state space from 0,1,2,3 to 0,1,2,3,4,5, for example. It remains a decision on which predictors to use and their functional form and how they influence the transition rates.

Acknowledgments
This work was accomplished while E. C.-B. was a post doctoral fellow of the Pacific Institute for Mathematical Sciences. This research of B. K. is funded by a grant from the Natural Sciences and Engineering Research Council of Canada. The research of C. S. was supported in part by NSF grant AGS-1062217 and DOE grant DE-SC0016245. The two DYNAMO data sets used in this study can be dowloaded through the DYNAMO Legacy repository (http://dynamo.fl-ext.ucar.edu/dynamo_legacy/).

References

Ajayamohan, R. S., Khouider, B., Majda, A. J., & Deng, Q. (2016). Role of stratiform heating on the organization of convection over the monsoon trough. *Climate Dynamics*, *47*(12), 3641–3660. https://doi.org/10.1007/s00382-016-3033-7

Benedict, J. J., & Randall, D. A. (2007). Observed characteristics of the MJO relative to maximum rainfall. *Journal of the Atmospheric Sciences*, *64*(7), 2332–2354.

Bergemann, M., & Jakob, C. (2016). How important is tropospheric humidity for coastal rainfall in the tropics? *Geophysical Research Letters*, *43*, 5860–5868. https://doi.org/10.1002/2016GL069255

Bergemann, M., Khouider, B., & Jakob, C. (2017). Coastal tropical convection in a stochastic modeling framework. *Journal of Advances in Modeling Earth Systems*, *9*, 2561–2582. https://doi.org/10.1002/2017MS001048

Bony, S., & Dufresne, J. L. (2005). Marine boundary layer clouds at the heart of tropical cloud feedback uncertainties in climate models. *Geophysical Research Letters*, *32*, L20806. https://doi.org/10.1029/2005GL023851

Bony, S., Stevens, B., Coppin, D., Becker, T., Reed, K., Voigt, A., & Medeiros, B. (2016). Thermodynamic control of anvil cloud amount. *Proceedings of the National Academy of Sciences of the United States of America*, *113*(32), 8927–8932.

Brenowitz, N. D., & Bretherton, C. S. (2018). Prognostic validation of a neural network unified physics parameterization. *Geophysical Research Letters*, *45*, 6289–6298. https://doi.org/10.1029/2018GL078510

Brient, F., & Bony, S. (2013). Interpretation of the positive low-cloud feedback predicted by a climate model under global warming. *Climate Dynamics*, *40*(9-10), 2415–2431.

Bright, D. R., & Mullen, S. L. (2002). Short-range ensemble forecasts of precipitation during the Southwest Monsoon. *Weather Forecasting*, *7*(5), 1080–1100.

Buizza, R., Miller, M., & Palmer, T. N. (1999). Stochastic representation of model uncertainties in the ECMWF Ensemble Prediction System. *Quarterly Journal of the Royal Meteorological Society*, *125*, 2887–2908.

Ceppi, P. Z. M., Brient, F., Zelinka, M. D., & Hartmann, D. L. (2017). Cloud feedback mechanisms and their representation in global climate models. *Wiley Interdisciplinary Reviews-Climate Change*, *8*, e465.

Ciesielski, P. E., Johnson, R. H., Haertel, P. T., & Wang, J. (2003). Corrected TOGA COARE sounding humidity data: Impact on diagnosed properties of convection and climate over the warm pool during MISMO. *Journal of Climate*, *16*, 2370–2384.

Crueger, T., & Stevens, B. (2015). The effect of atmospheric radiative heating by clouds on the Madden-Julian Oscillation. *Journal of Advances in Modeling Earth Systems*, *7*, 854–864. https://doi.org/10.1002/2015MS000434

De La Chevrotière, M., Khouider, B., & Majda, A. J. (2014). Calibration of the stochastic multicloud model using Bayesian inference. *SIAM Journal on Scientific Computing*, *36*(3), B538–B560.

De La Chevrotière, M., Khouider, B., & Majda, A. J. (2016). Stochasticity of convection in Giga-LES data. *Climate Dynamics*, *47*, 1845–1861.

Deng, Q., Khouider, B., & Majda, A. (2015). The MJO in a coarse-resolution GCM with a stochastic multicloud parameterization. *Journal of the Atmospheric Sciences*, *72*, 55774. https://doi.org/10.1175/JAS-D-14-0120.1

Deng, Q., Khouider, B., Majda, A., & Ajayamohan, R. (2016). Effect of stratiform heating on the planetary-scale organization of tropical convection. *Journal of the Atmospheric Sciences*, *73*, 371–392. https://doi.org/10.1175/JAS-D-15-0178.1

Donner, L. J. (1993). A cumulus parameterization including mass fluxes, vertical momentum dynamics, and mesoscale effects. *Journal of the Atmospheric Sciences*, *50*, 889–906.

Dorrestijn, J., Crommelin, D., Biello, J., & Boing, S. (2013). A data-driven multicloud model for stochastic parameterization of deep convection. *Philosophical Transactions of the Royal Society A*, *371*, 20120374.

Emanuel, K. A., & Raymond, D. J. (1993). The representation of cumulus convection in numerical models. *Meteorological Monographs*, *46*, 1–246. https://doi.org/10.1175/0065-9401-24.46.1

Feng, Z., McFarlane, S. A., Schumacher, C., Ellis, S., & Bharadwaj, N. (2014). Constructing a merged cloud-precipitation radar dataset for tropical convective clouds during the DYNAMO/AMIE experiment at Addu Atoll. *Journal of Atmospheric and Oceanic Technology*, *31*, 1021–1042.

Fliegel, J. (2011). Quality control and census of SMART-R observations from the DYNAMO/CINDY2011 field campaign, Thesis, Office of. Graduate Studies of Texas A & M.

Frenkel, Y., Majda, A., & Khouider, B. (2012). Using the stochastic multicloud model to improve tropical convective parameterization: A paradigm example. *Journal of the Atmospheric Sciences*, *69*, 1080–1105.

Gentine, P., Pritchard, M., Rasp, S., Reinaudi, G., & Yacalis, G. (2018). Could machine learning break the convection parameterization deadlock? *Geophysical Research Letters*, *45*, 5742–5751. https://doi.org/10.1029/2018GL078202

Gettleman, A., & Sherwood, S. C. (2016). Process responsible for cloud feedback. *Current Climate Change Reports*, *32*, 179C–189.

Gillespie, D. T. (1975). An exact method for numerically simulating the stochastic coalescence process in a cloud. *Journal of the Atmospheric Sciences*, *32*, 1977–1989.

Goswami, B. B., Khouider, B., Krishna, R. P. M., Mukhopadhyay, P., & Majda, A. J. (2017a). Implementation and calibration of a stochastic convective parameterization in the NCEP Climate Forecast System. *Journal of Advances in Modeling Earth Systems*, *9*, 1721–1739. https://doi.org/10.1002/2017MS001014

Goswami, B. B., Khouider, B., Krishna, R. P. M., Mukhopadhyay, P., & Majda, A. J. (2017b). Improved tropical modes of variability in the NCEP climate forecast system (version 2) via a stochastic multicloud model. *Journal of the Atmospheric Sciences*, *74*, 3339–3366. https://doi.org/10.1175/JAS-D-17-0113.1

Goswami, B. B., Khouider, B., Krishna, R. P. M., Mukhopadhyay, P., & Majda, A. J. (2017c). Improving synoptic and intraseasonal variability in CFSv2 via stochastic representation of organized convection. *Geophysical Research Letters*, *44*, 1104–1113. https://doi.org/10.1002/2016GL071542

Gottschalck, J., Roundy, P. E., Schreck III, C. J., Vintzileos, A., & Zhang, C. (2013). Large-scale atmospheric and oceanic conditions during the 2011–12 DYNAMO field campaign. *Monthly Weather Review*, *141*(12), 4173–4196. https://doi.org/10.1175/MWR-D-13-00022.1

Haertel, P. T., Kiladis, G. N., Denno, A., & Rickenbach, T. M. (2008). Vertical-mode decompositions of 2-day waves and the Madden-Julian Oscillation. *Journal of the Atmospheric Sciences*, *65*(3), 813–833.

Hagos, S., Feng, Z., Plant, R. S., Houze, R. A. Jr, & Xiao, H. (2018). A stochastic framework for modeling the population dynamics of convective clouds. *Journal of Advances in Modeling Earth Systems*, *10*, 448–465. https://doi.org/10.1002/2017MS001214

Hartmann, D. L. (2016). Tropical anvil clouds and climate sensitivity. *Proceedings of the National Academy of Sciences of the United States of America*, *113*(32), 8897–8899.

Heidelberger, P., & Welch, P. D. (1981). A spectral method for confidence interval generation and run length control in simulations. *Communications of the ACM*, *24*, 233–245.

Henderson, S. A., Maloney, E. D., & Son, S. W. (2017). Madden-Julian Oscillation Pacific teleconnections: The impact of the basic state and MJO representation in general circulation models. *Journal of Climate*, *30*, 4567–4587.

Hendon, H. H. (1993). The diurnal cycle of tropical convection. *Journal of Geophysical Research*, *98*, 16,623–16,637.

Hendon, H. H., & Liebmann, B. (1990). The intraseasonal (30-50 day) oscillation of the Australian summer monsoon. *Journal of the Atmospheric Sciences*, *47*, 2909–2923.

Hendon, H. H., Wheeler, M. C., & Zhang, C. (2007). Seasonal dependence of the MJO-ENSO relationship. *Journal of the Atmospheric Sciences*, *20*(3), 531–543.

Hohenegger, C., & Stevens, B. (2013). Preconditioning deep convection with cumulus congestus. *Journal of the Atmospheric Sciences*, *70*, 448–464.

Holton, J. R. (1972). *An introduction to dynamic meteorology*. New York: Academic Press.

Hung, M. P., Lin, J. L., Wang, W., Kim, D., Shinoda, T., & Weaver, S. J. (2013). MJO and convectively coupled equatorial waves simulated by CMIP5 climate models. *Journal of Climate*, *26*(17), 6185–6214.

IPCC (2007). Climate Change 2007: The Physical Science Basis. Summary for Policymakers. In S. Solomon et al. (Ed.), *Contribution of Working Group I to the fourth assessment report of the Intergovernmental Panel on Climate Change*. Cambridge: Cambridge University Press.

IPCC (2013). Climate change 2013: The physical science basis. In T. F. Stocker, D. Qin, G.-K. Plattner, M. Tignor, S. K. Allen, & J. Boschung (Eds.), *Contribution of Working Group I to the fifth assessment report of the Intergovernmental Panel on Climate Change*. Cambridge: Cambridge University Press.

Jakob, C. (2001). The representation of cloud cover in atmospheric general circulation models (PhD thesis), Ludwig-Maximilians-Universitaet Muenchen.

Järvinen, H., Laine, M., Solonen, A., & Haario, H. (2012). Ensemble prediction and parameter estimation system: The concept. *Quarterly Journal of the Royal Meteorological Society*, *138*(663), 281–288. https://doi.org/10.1002/qj.923

Johnson, R. H., & Ciesielski, P. E. (2013). Structure and properties of Madden-Julian Oscillations deduced from DYNAMO sounding arrays. *Journal of the Atmospheric Sciences*, *70*(10), 3157–3179. https://doi.org/10.1175/JAS-D-13-065.1

Johnson, R. H., & Lin, X. (1997). Episodic trade wind regimes over the western Pacific warm pool. *Journal of the Atmospheric Sciences*, *54*, 2020–2034.
Johnson, R. H., Rickenbach, T. M., Rutledge, S. A., Ciesielski, P. E., & Schubert, W. H. (1999). Trimodal characteristics of tropical convection. *Journal of Climate*, *12*(8), 2397–2418.
Kain, J. S., & Fritsch, J. M. (1990). A one-dimensional entraining/detraining plume model and its application in convective parameterization. *Journal of the Atmospheric Sciences*, *47*, 2784–2802.
Katsumata, M., Ciesielski, P. E., & Johnson, R. H. (2011). Evaluation of budget analysis during MISMO. *Journal of Applied Meteorology and Climatology*, *40*, 241–254.
Keane, R. J., Plant, R. S., & Tennant, W. J. (2016). Evaluation of the Plant-Craig stochastic convection scheme (v2.0) in the ensemble forecasting system MOGREPS-R (24 km) based on the Unified Model (v7.3). *Geoscientific Model Development*, *9*, 1921–1935.
Khairoutdinov, M. F., Krueger, S. K., Moeng, C. H., Bogenschutz, P. A., & Randall, D. A. (2009). Large-eddy simulation of maritime deep tropical convection. *Journal of Advances in Modeling Earth Systems*, *1*, 15. https://doi.org/10.3894/JAMES.2009.1.15
Khouider, B. (2014). A coarse grained stochastic multi-type particle interacting model for tropical convection: Nearest neighbour interactions. *Communications in Mathematical Sciences*, *12*, 1379–1407.
Khouider, B., Biello, J., & Majda, A. J. (2010). A stochastic multicloud model for tropical convection. *Communications in Mathematical Sciences*, *8*(1), 187–216.
Khouider, B., & Majda, A. J. (2006a). Model multi-cloud parameterizations for convectively coupled tropical waves: Detailed nonlinear wave evolution. *Dynamics of Atmospheres and Oceans*, *42*, 59–80.
Khouider, B., & Majda, A. J. (2006b). A simple multicloud parameterization for convectively coupled tropical waves. Part I: Linear analysis. *Journal of the Atmospheric Sciences*, *63*, 1308–1323.
Khouider, B., & Majda, A. J. (2008a). Equatorial convectively coupled waves in a simple multicloud model. *Journal of the Atmospheric Sciences*, *65*, 3376–3397.
Khouider, B., & Majda, A. J. (2008b). Multicloud model for organized tropical convection: Enhanced congestus heating. *Journal of the Atmospheric Sciences*, *65*, 895–914.
Khouider, B., Majda, A. J., & Stechmann, S. N. (2013). Climate science in the tropics: Waves, vortices, and PDEs. *Nonlinearity*, *26*, R1–R68.
Khouider, B., Majda, A., & Katsoulakis, M. (2003). Coarse grained stochastic models for tropical convection and climate. *Proceedings of the National Academy of Sciences of the United States of America*, *100*, 11,941–11,946.
Kidd, C., Dawkins, E., & Huffman, G. (2013). Comparison of precipitation derived from the ECMWF operational forecast model and satellite precipitation datasets. *Journal of Hydrometeorology*, *14*, 1463–1482.
Kikuchi, K., & Takayabu, Y. (2004). The development of organized convection associated with the MJO during TOGA COARE IOP: Trimodal characteristics. *Geophysical Research Letters*, *31*, L10101. https://doi.org/10.1029/2004GL019601
Klein, S. A., Hall, A., Norris, J. R., & Pincus, R. (2017). Low-cloud feedbacks from cloud-controlling factors: A review. *Surveys in Geophysics*, *38*, 1307C1329.
Klotzbach, P. J., & Oliver, E. (2014). The Madden-Julian Oscillation's impacts on worldwide tropical cyclone activity. *Journal of Climate*, *27*, 2317–2330.
Kumar, V. V., Jakob, C., Protat, A., May, P. T., & Davies, L. (2013). The four cumulus cloud modes and their progression during rainfall events: A C-band polarimetric radar perspective. *Journal of Geophysical Research: Atmospheres*, *118*, 8375–8389. https://doi.org/10.1002/jgrd.50640
Lawrence, D. M., & Webster, P. J. (2002). The boreal summer intraseasonal oscillation: Relationship between northward and eastward movement of convection. *Journal of the Atmospheric Sciences*, *59*, 1593–1606.
Liebmann, B., Hendon, H. H., & Glick, J. D. (1994). The relationship between tropical cyclones of the Western Pacific and Indian Oceans and the Madden-Julian Oscillation. *Journal of the Meteorological Society of Japan*, *72*, 401–412.
Lin, J. L., Kiladis, G. N., Mapes, B. E., Weickmann, K. M., Sperber, K. R., Lin, W., et al. (2006). Tropical intraseasonal variability in 14 IPCC AR4 climate models. Part I: Convective signals. *Journal of Climate*, *19*(12), 2665–2690.
Lin, J., & Neelin, J. D. (2002). Considerations for stochastic convective parameterization. *Journal of the Atmospheric Sciences*, *59*(5), 959–975.
Lin, J., & Neelin, J. D. (2003). Toward stochastic deep convective parameterization in general circulation models. *Geophysical Research Letters*, *30*(4), 1162. https://doi.org/10.1029/2002GL016203
Majda, A. J., & Shefter, M. (2001). Models for stratiform instability and convectively coupled waves. *Journal of the Atmospheric Sciences*, *58*, 1567–1584.
Mapes, B. E. (2000). Convective inhibition, subgridscale triggering energy, and "stratiform instability" in a toy tropical wave model. *Journal of the Atmospheric Sciences*, *57*, 1515–1535.
Mapes, B., & Houze Jr, R. A. (1992). An integrated view of the 1987 Australian monsoon and its mesoscale convective systems. I: Horizontal structure. *Quarterly Journal of the Royal Meteorological Society*, *118*, 927–963.
Mapes, B., Tulich, S., Lin, J., & Zuidema, P. (2006). The mesoscale convection life cycle: Building block or prototype for large-scale tropical waves? *Dynamics of Atmospheres and Oceans*, *42*(1-4), 3–29.
McCoy, D. T., Eastman, R., Hartmann, D. L., & Wood, R. (2017). The change in low cloud cover in a warmed climate inferred from AIRS, MODIS, and ERA-Interim. *Journal of Climate*, *30*(10), 3609–3620. https://doi.org/10.1175/JCLI-D-15-0734.1
McCoy, D. T., Hartmann, D. L., Zelinka, M. D., Ceppi, P., & Grosvenor, D. P. (2015). Mixed-phase cloud physics and Southern Ocean cloud feedback in climate models. *Journal of Geophysical Research: Atmospheres*, *120*, 9539–9554. https://doi.org/10.1002/2015JD023603
Morita, J., Takayabu, Y. N., Shige, S., & Kodama, Y. (2006). Analysis of rainfall characteristics of the Madden-Julian Oscillation using TRMM satellite data. *Dynamics of Atmospheres and Oceans*, *42*, 107–126.
Nuss, W. A., & Titley, D. W. (1994). Use of muliquadric interpolation for meteorological objective analysis. *Monthly Weather Review*, *122*, 1611–1631.
Palmer, T. N. (2001). A nonlinear dynamical perspective on model error: A proposal for non-local stochastic-dynamic parametrization in weather and climate prediction models. *Quarterly Journal of the Royal Meteorological Society*, *127*, 279–304.
Peters, K., Crueger, T., Jakob, C., & Möbis, B. (2017). Improved MJO-simulation in ECHAM6.3 by coupling a stochastic multicloud model to the convection scheme. *Journal of Advances in Modeling Earth Systems*, *9*, 193–219. https://doi.org/10.1002/2016MS000809
Peters, K., Jakob, C., Davies, L., Khouider, B., & Majda, A. (2013). Stochastic behavior of tropical convection in observations and a multicloud model. *Journal of the Atmospheric Sciences*, *70*, 3556–3575. https://doi.org/10.1175/JAS-D-13-031.1
Plant, R., & Craig, G. (2008). A stochastic parameterization for deep convection based on equilibrium statistics. *Journal of the Atmospheric Sciences*, *65*(1), 87–105.
Rasp, S., Pritchard, M. S., & Gentine, P. (2018). Deep learning to represent subgrid processes in climate models. *Proceedings of the National Academy of Sciences of the United States of America*, *115*, 9684–9689.

Ruppert, J., & Johnson, R. (2015). Diurnally modulated cumulus moistening in the preonset stage of the Madden–Julian oscillation during DYNAMO. *Journal of the Atmospheric Sciences*, *72*, 162271647. https://doi.org/10.1175/JAS-D-14-0218.1

Schneider, T., Lan, S., Stuart, A., & Teixeira, J. (2017). Earth system modeling 2.0: A blueprint for models that learn from observations and targeted high-resolution simulations. *Geophysical Research Letters*, *44*, 12,396–12,417. https://doi.org/10.1002/2017GL076101

Senior, C. A., & Mitchell, J. F. B. (1993). CO_2 and climate: The impact of cloud parametrizations. *Journal of Climate*, *6*, 393–418.

Sherwood, S. C. (1999). Convective precursors and predictability in the tropical western Pacific. *Monthly Weather Review*, *127*, 2977–2991.

Siebesma, A. P., Jakob, C., Lenderink, G., Neggers, R., Teixeira, J., Calvo, J., et al. (2004). Cloud representation in General Circulation Models over the Northern Pacific Ocean: A EUROCS intercomparison study. *Quarterly Journal of the Royal Meteorological Society*, *130*, 3245–3267.

Steiner, M., Houze, R. A., Jr. & Yuter, S. E. (1995). Climatological characterization of three-dimensional storm structure from operational radar and rain gauge data. *Journal of Applied Meteorology and Climatology*, *34*, 1978–2007.

Stephens, G. L. (2005). Cloud feedbacks in the climate system: A critical review. *Journal of Climate*, *18*, 237–273.

Tsushima, Y., Brient, F., Klein, S. A., Konsta, D., Nam, C., Qu, X., et al. (2017). The cloud feedback model intercomparison project (CFMIP) diagnostic codes catalogue: Geoscientific model development. *Journal of the Atmospheric Sciences*, *10*(11), 4285–4305.

Waite, M., & Khouider, B. (2010). The deepening of tropical convection by congestus preconditioning. *Journal of the Atmospheric Sciences*, *67*, 2601–2615.

Webb, M. J., Andrews, T., Bodas-Salcedo, A., Bony, S., Bretherton, C. S., Chadwick, R., et al. (2016). The cloud feedback model Intercomparison Project (CFMIP) contribution to CMIP6. *Geoscientific Model Development*, *10*(1), 359–384.

Webb, M. J., Lock, A. P., Bretherton, C. S., Bony, S., Cole, J. N. S., Idelkadi, A., et al. (2015). The impact of parametrized convection on cloud feedback. *Philosophical Transactions of the Royal Society of London. Series A*, *373*(2054), 20140414.

Webster, P. J., & Lukas, R. (1992). TOGA COARE: The coupled ocean-atmosphere response experiment. *Bulletin of the American Meteorological Society*, *73*(9), 1377–1416. https://doi.org/10.1175/1520-0477(1992)073<1377:TCTCOR>2.0.CO;2

Yoneyama, K., Zhang, C., & Long, C. N. (2013). Tracking pulses of the Madden-Julian Oscillation. *Bulletin of the American Meteorological Society*, *94*, 1871–1891. https://doi.org/10.1175/BAMS-D-12-00157.1

Zelinka, M. D., Klein, S. A., & Hartmann, D. L. (2012). Computing and partitioning cloud feedbacks using cloud property histograms. Part II: Attribution to changes in cloud amount, altitude, and optical depth. *Journal of Climate*, *25*, 3736–3754.

Zhang, C. (2005). Madden–Julian oscillation. *Reviews of Geophysics*, *43*, RG2003. https://doi.org/10.1029/2004RG000158

Zhang, C. (2013). "Madden-Julian Oscillation": Bridging weather and climate. *Bulletin of the American Meteorological Society*, *94*(12), 1849–1870. https://doi.org/10.1175/BAMS-D-12-00026.1

Zhang, C., Gottschalck, J., Maloney, E. D., Moncrieff, M. W., Vitart, F., Waliser, D. E., et al. (2013). Cracking the MJO nut. *Geophysical Research Letters*, *40*, 1223–1230. https://doi.org/10.1002/grl.50244

Zhang, Y., Klein, S. A., Mace, G. C., & Boyle, J. (2010). Evaluation of tropical cloud and precipitation statistics of Community Atmosphere Model version 3 using CloudSat and CALIPSO data. *Journal of Geophysical Research*, *115*, D12205. https://doi.org/10.1029/2009JD012006

Zhang MH, B. C. (2008). Mechanisms of low cloud-climate feedback in idealized single-column simulations with the community atmospheric model. *Journal of Climate*, *21*(21), 4859–4878.

Zhao, M., Golaz, J.-C., Held, I. M., Ramaswamy, V., Lin, S. J., Ming, Y., et al. (2016). Uncertainty in model climate sensitivity traced to representations of cumulus precipitation microphysics. *Journal of Climate*, *29*, 543–560. https://doi.org/10.1175/JCLI-D-15-0191.1